MOLECULAR SIMULATION STUDY OF THE CORRELATIONS BETWEEN DIBLOCK COPOLYMER MICROSTRUCTURE AND TRANSPORT PROPERTIES

A Thesis

Presented to the Faculty of the Graduate School

of Cornell University

in Partial Fulfillment of the Requirements for the Degree of

Master of Science

by

Mohammed Suliman Alshammasi

August 2018

ABSTRACT

Diblock copolymers (DBPs) are used in numerous current and potential applications, from composite materials to electrolyte membranes. Depending on the chemical incompatibility of the blocks and their volume fractions, they self-segregate into microdomains inducing anisotropy and different symmetries to the microstructure, resulting in significant variability in the macroscopic properties.

DBPs are emerging as a candidate for replacing conventional liquid electrolytes in electrochemical devices, due to their improved chemical and mechanical stability. In contrast to isotropic melts, the self-segregation of DBPs allows the decoupling of ionic transport and mechanical properties. In this work, molecular dynamic simulations of coarse-grained DBPs were devised and carried out to unveil correlations between the microstructure and both ionic mobility (μ), and dynamics/viscoelasticity (directly correlate with mechanical properties) of DBPs.

It was found that across different morphologies and chain lengths (N), μ is mainly controlled by the extent of microdomains mixing and the tortuosity of the conductive path. Furthermore, the local fluctuations in the density of the polymer matrix have a non-negligible effect on the transport of ions.

Our study of dynamic and viscoelastic properties of DBPs revealed that the interface between the two blocks constrains chain conformations in a way akin to topological constraints caused by entanglements. Specifically, the DBP interface gives rise to a temperature-dependent early crossover from Rouse to reptation scaling of the self-diffusion coefficient with N compared to isotropic melts.

Rheologically, the interface manifests into a modulus plateau similar to that of the rubbery plateau of entangled polymer melts that arises at the same Rouse to reptation scaling crossover N.

Overall, the results of this study shed some light on the effects of various design and operating parameters, such as block composition, temperature, and external forces, on the transport properties of DBPs. It is expected that these results will provide a fundamental basis to complement ongoing experimental and modeling efforts devoted to engineer DBPs for target applications.

BIOGRAPHICAL SKETCH

The author, Mohammed Suliman AlShammasi was born in Jubail, Saudi Arabia to Suliman Mohammed AlShammasi and Wafa Rasool AlKhunaizi in 1990. He was raised for most of his life in Qatif, Saudi Arabia where he completed his elementary, middle, and high school in 2007. Upon completing his high school, Mohammed was awarded a scholarship by the government of Saudi Arabia and Saudi Aramco to complete his Bachelor of Science in chemical and life science engineering at Virginia Commonwealth University. Upon graduation in 2013, he joined the Chemicals Admin Area of Saudi Aramco where he completed several training assignments related to project management and process engineering.

As part of the Advanced Degree Program of Saudi Aramco, Mohammed was offered the opportunity to pursue his Master of Science in chemical engineering with emphasis in polymers at Cornell University, where he joined Professor Fernando Escobedo's group in 2016.

Under Professor Escobedo's supervision, Mohammed worked toward understanding the structure-property relationship of diblock copolymer systems. Mainly, studying the effect of microstructure on ionic mobility, dynamic and viscoelastic properties via utilizing Molecular Dynamic (MD) simulations.

In memory of my father Suliman Mohammed AlShammasi (1957–1996), my grandfather Rasool Ali AlKhunaizi (–2006), and my grandmother Naeema Ahmed AlMustafa (–2016).

To my mother Wafa Rasool AlKhunaizi with love and eternal appreciation.

ACKNOWLEDGEMENTS

Just like the cooperative motion of polymer segments near the glass transition temperature, our cooperation and collaboration are the distinctive features of our human race. It is the unique interactions with our peers that lead to our development as individuals and as societies. This work is a refined product of many fruitful interactions with individuals of different scientific backgrounds to whom I am grateful.

The completion of this work would not have been possible without the continued support of my adviser, Professor Fernando A. Escobedo. I greatly appreciate his patience, encouragements, enthusiasm about research, and for sharing his immense knowledge in thermodynamics and polymers physics throughout my master's residency.

I would like to thank Professor Christopher K. Ober for serving as a member in my master's committee despite his busy schedule, and for insightful discussions during the Designing Materials to Revolutionize and Engineer our Future (DMREF) project meetings and thesis defense.

I would like to thank the Escobedo's Group members especially, Chris Nowak for teaching me from day one how to perform and analyze simulations, Mohammed AlHashim for his good friendship and challenging fundamental questions in all aspects of life, Prajwal BP, and Dr. Mayank Misra for the useful discussions and constructive criticism.

I am forever indebted to my mother for her unlimited care, unconditional love, and encouragement throughout my life. This work is your achievement as much as it is mine, thank you mom. I am greatly thankful to my wife, Hawra Mohammed AlSuliman for her constant love, patience, encouragement, and above all, for assuming complete responsibility of our son, Nasser, in the past

two years. I am thankful to my elder brother, Mishal, and younger sister, Fatima, for always being supportive. I am utterly thankful to my uncles, Naseem, Osama, Loay, and Ali, and my aunt, Eshraq AlKhunaizi for being a constant source of comfort and security. My in-laws, Mohammed Taha AlSuliman and Azhar Ahmed AlJishi unconditional support to my family and devotion to caring for Nasser were the key for myself and my wife to pursue our aspirations; words cannot describe my gratitude.

I acknowledge my employer and sponsor, Saudi Aramco, for giving me the opportunity to pursue my master's degree in a subject I am very passionate about hoping that I will use what I learned to positively contribute in the development of the company.

Last but not least, I would like to thank the one and only, the Almighty Allah, for creating a complex universe that can be studied and explained by elegant physical laws.

TABLE OF CONTENTS

LIST OF TABLES

LIST OF FIGURES

CHAPTER 1

INTRODUCTION

1.1 Overview

Polymers, a sub-class of macromolecules, consist of a large number of covalently bonded repeat units (i.e., monomers), the number of which is the degree of polymerization (N). Homopolymers, as the name suggests, are made of one type of monomers and can be synthesized into linear, branched, ring, dendrimer (i.e. tree-like) structures, and cross-linked networks. Another important class of synthetic polymers is heteropolymers which consist of two or more types of monomers. For the copolymer case (i.e., two monomer types), depending on the relative reactivity of the monomers (i.e., between the same monomer type versus different monomer types), alternating, block, and random copolymers can be synthesized. This thesis is focused on linear diblock copolymers (DBP) due to their appealing properties which stem from the rich phase behavior in the melt state.

Depending on the volume fraction of the constitutive blocks (ϕ_1), their chemical incompatibility (i.e., Flory-Huggins parameter, χ), and N, a DBP in the melt state can form a microphase separated structure that minimizes the free energy of the system as shown in an ideal DBP phase diagram in Figure 1.1a [1]. A depiction of the different morphologies of DBP is shown in Figure 1.1b. The microphase separation induces anisotropy and different symmetries to the microstructure of DBPs resulting in changes to their macroscopic properties. This microphase separation gives rise to hybrid materials with interesting conflicting properties making them attractive in applications ranging from lithogra-

phy, to artificial organs technology, drug delivery, and energy storage [3]. For example, the mechanical stability of solid polymers electrolyte (SPE) used in battery applications is essential for sustainable and safe operations [4]. DBPs have been thoroughly studied as a potential materials platform to improve SPE stability and safety [5–7]. While the conductive block is flexible and contains polar sites that can solvate salts and facilitate ions transport, making the other non-conductive block rigid or glassy imparts the system with the mechanical stability needed to suppress dendrite formation, a deficiency that causes fire. In drug delivery applications, blocks with different hydrophobicity can be utilized in order to transport hydrophobic drugs in the bloodstream at concentrations above their intrinsic water solubility limit. The hydrophilic block forms a protective shell for the bioactive molecules against bio-degradation enhancing the drug integrity and performance. Additionally, the reversible nature of the DBPs ordering (i.e., from order to disorder and vice versa by changing the operating temperature) allows for controlled release of the drug [8].

Recently, experimental and computational studies have shown that the ionic conductivity increases with molecular weight of Lamellae-forming DBPs in contrast to the homopolymer case where the ionic conductivity decreases with molecular weight. The conductivity decrease in the latter was attributed to a reduced segmental motion of the polymer chain [9,10]. The increase in conductivity in the DBP case was found to be related to an increase in the thickness of the conductive domain relative to the interface thickness. It was hypothesized that ionic conductivity is low near the interface due to either its proximity to the glassy domain [9], or/and the presence of a conductive/non-conductive mixture zone [10,11].

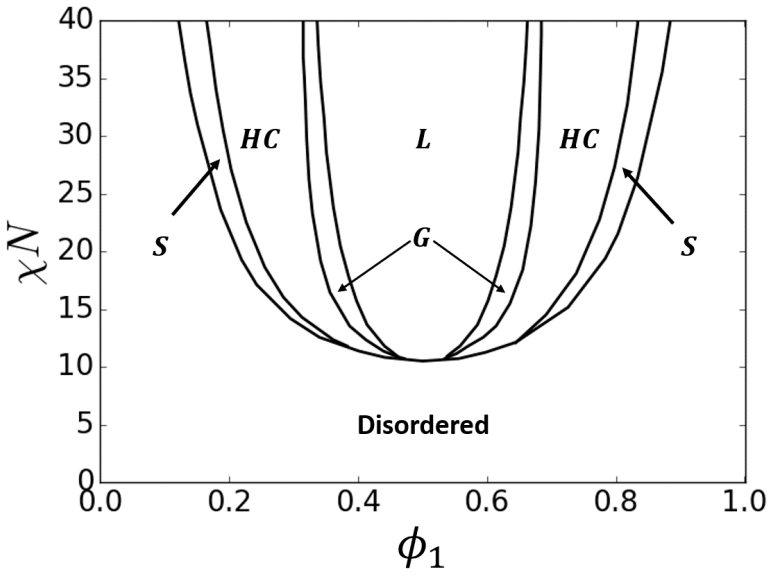

(a)

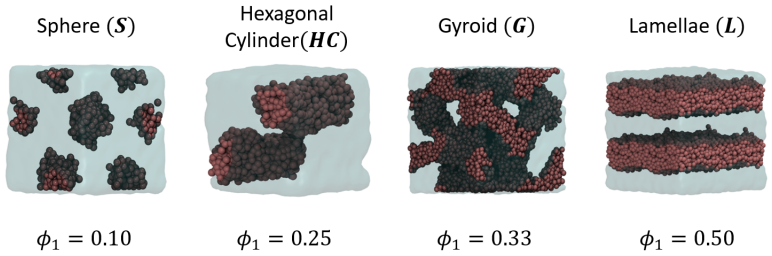

(b)

Figure 1.1: (a) DBP ideal phase diagram as obtained from Self-consistent field theory (SCFT) [1]. (b) A depiction of the different morphologies obtained by varying ϕ_1, where the minority block is represented by the brown beads.

To date, only few experimental studies have investigated the effect of DBP morphology on ionic conductivity. One key property of the polymer matrix that largely influences ionic conductivity is the domain orientation across grain boundaries [12], which is dictated by the nucleation mechanism of the phase. These studies posit that a DBP with a 3D morphology (like the Gyroid, *G*, and majority component of a Hexagonal Cylinder, *HC*) would yield the highest conductivity [7, 13]. However, given the variable effect of grain boundaries and

structural defects, it is difficult to assess the isolated effect of morphology on ionic conductivity within an experimental framework [7].

Another important feature of SPEs is their mechanical stability, which, to some extent, is improved by utilizing DBPs. The dynamic and viscoelastic properties of a polymer correlates with its mechanical stability and strength. While the dynamic and viscoelastic properties and their dependence on a wide spectrum of parameter space is well understood for homopolymer melt systems, the mechanism and governing factors that influence the subject properties require further explanations and understanding in DBP systems. The introduction of interfaces due to the chemical incompatibility of the constituent blocks, gives rise to additional energetic and entropic barriers that influence the dynamic and viscoelastic properties of the DBPs.

1.2 Simulations

One key property of the DBP matrix that largely influences its structure, and by virtue its properties, is the domains orientations across grain boundaries. Varieations in grain orientations and sizes present in randomly oriented experimental systems can lead to debatable interpretions of trends especially that of transport properties [7, 12]. This limitation gives advantage to utilizing molecular simulation techniques to study defect- and grain-boundary-free structures conventionally. Molecular Dynamic (MD) simulations can be effectively used to theoretically resolve and clarify the different mechanisms underlying dynamic and viscoelastic properties of polymeric materials from a microscopic perspective.

MD simulations have been used to study the dynamic, static, and kinetics properties of biological, organic, electronic, and polymeric materials in different length and time scales. In MD, a system is fully described by a set of interaction potentials, an initial configuration, and initial velocities. The underlying working principle of MD is to iteratively solve Newton's equations of motion both in space ($\boldsymbol{r}^N$) and time (t) numerically. In this work, pairwise additivity for non-bonded interactions is assumed, such that the potential energy of particle i (U_i) is the summation of its interactions with other particles (j) in the system:

$$U_i = \sum_{j(j \neq i)} U_{ij}(r_{ij}) \tag{1.1}$$

where r_{ij} is the distance between atoms i and j.

Given a set of bonded and non-bonded interaction potentials, the forces between atoms are computed:

$$\vec{f_i} = -\nabla U_i \tag{1.2}$$

where:

$$U_i = U_i(\text{itramolecular}) + U_i(\text{iteramolecular}) \tag{1.3}$$

and accordingly their positions and velocity are evaluated for a long time in order for the system to reach its equilibrium state before calculations (i.e., production run) are performed.

For computational efficiency, coarse-grained representation of the polymer is adopted. In coarse-grained representation, multiple repeat-units are represented by a single bead and effective interaction parameters. Typically, a bead size represents a Kuhn length of the polymer. General coarse-grained MD is useful in studying universal properties of polymers which are independent of the specific chemistry.

1.3 Thesis Outline

In Chapter 2, the effects on ionic mobility (μ) of morphology (i.e., of varying path tortuosity of the conductive domain) and the extent of microdomains mixing at the nano-scale are investigated. It is shown that the addition of a second conductive block induces low-density regions that can be exploited as a design strategy for enhanced μ and mechanical stability in SPE.

In Chapter 3, the effect of DBP morphology in various transport properties is examined. It is shown that depending on temperature, the DBP crosses from the Rouse regime to the reptation regime at a shorter chain length compared to homopolymer, which is attribute to the topological constraint imposed by the interface between the two blocks that also gives rise to entanglement-like rheological signature (i.e., a plateau modulus). It is also demonstrated that block-retraction, similar to arm retraction in star polymers, is essential to activate the lateral diffusion process for high chain lengths DBPs.

The methodology adapted in this thesis for studying mechanical and rheological properties relied on macroscopic deformation of the structure. Another non-invasive method for extracting rheological information at the nano-scale is presented in the future work in Chapter 4. Mainly, nanoparticles dynamics can be traced to extract rheological information at different length scales depending on the nanoparticles size and the characteristic length scales the define the polymer structure. Implications and relevance to emerging applications for using such method is also presented.

CHAPTER 2

CORRELATIONS BETWEEN IONIC MOBILITY AND BLOCK COPOLYMERS MICROSTRUCTURE

2.1 Abstract

Molecular simulations of coarse-grained diblock copolymers (DBP) were devised to unveil correlations between microstructure and ionic mobility (μ). It is found that three key microstructural features had a significant effect on ion transport: the extent of microdomains mixing (β), the tortuosity of the conductive domain (λ), and the local fluctuations in the density (ρ) of the polymer matrix. While the β effect has been previously studied in some detail for Lamellae morphology, the effect of ρ non-homogeneities, and λ have received much less attention. To control the local fluctuations in ρ, a polymer design variant is explored that incorporates a second conductive block (A') that is incompatible with the other two blocks (A'-b-A-b-B). It is found that increasing the fraction of A' beads, increases the frequency and amplitude of the local ρ depleted regions within the conductive domain, resulting in an increase in μ. Additionally, the effect of morphology on μ was examined by varying the volume fraction of the constitutive blocks and utilizing the different blocks as the conductive domains. It is shown that μ for various defect-free morphologies and chain lengths can be correlated with β and λ via a single universal curve.

2.2 Introduction

Current safety and reliability concerns associated with conventional liquid electrolytes in battery applications have prompted a growing interest on the utilization of solid polymer electrolytes (SPE). The use of such materials could potentially mitigate electrolyte leakage, dendrite formation and consequently avoid short-circuiting in batteries [14].

Due to its ability to solvate salt and to provide conductive pathways that facilitate ion transport through a largely amorphous structure (at ambient conditions), polyethylene oxide (PEO) has been found to be one of the most suitable candidates as an SPE [6, 15]. However, to suppress dendrite growth, the shear modulus of the electrolyte should be significantly higher than that of the lithium electrode, a condition that is not met in neat PEO [4, 9, 16]. Diblock copolymers (DBP) have been studied as a potential materials platform to enhance the mechanical stability of SPEs. The conductive block, which is above its glass transition temperature (T_g) (e.g., PEO) imparts fast ionic transport, while the non-conductive block, that is typically below its T_g (e.g., polystyrene, PS) endows the system with the mechanical stability needed to suppress dendrite formation. Ion conducting and mechanical properties are also impacted by the specific morphology that DBPs may attain depending on the segregation strength (χN, where χ is the Flory-Huggins parameter accounting for the chemical non-compatibility of the blocks, and N is the total degree of polymerization), and the volume fractions of the minority block (ϕ_1)[17].

Recently, experimental and computational studies have shown that ionic conductivity increases with molecular weight of Lamellae-forming DBPs in con-

trast to the homopolymer case where ionic conductivity decreases with molecular weight. The ionic conductivity decrease in the latter was attributed to a reduced segmental motion of the polymer chain [9, 10]. The increase in ionic conductivity in the DBP case was found to be related to an increase in the thickness of the conductive domain relative to the interface thickness. It was hypothesized that ionic conductivity is low near the interface due to either its proximity to the glassy domain [9], or/and the presence of a conductive/non-conductive mixture zone [10, 11].

To date, only few experimental studies have investigated the effect of DBP morphology on ionic conductivity. One key property of the polymer matrix that largely influences the ionic conductivity is the domain orientation across grain boundaries [12], which is dictated by the nucleation mechanism of the phase. These studies posit that a DBP with a 3D morphology (like the Gyroid, *G*, and majority component of a Hexagonal Cylinder, *HC*) would yield the highest ionic conductivity [7, 13]. However, given the variable effect of grain boundaries and structural defects, it is difficult to assess the isolated effect of morphology on ionic conductivity within an experimental framework [7].

We study the effects on ionic mobility (μ) of morphology (i.e., of varying path tortuosity of the conductive domain) and the extent of microdomains mixing at the nano-scale. To provide the description of a reference, limiting behavior, only defect- and grain-boundary-free morphologies are considered. Additionally, we propose the addition of a second conductive block (A') that is incompatible with the other two blocks (A'-b-A-b-B) as a method of inducing low-density regions that can be exploited as a design strategy for enhanced μ and mechanical stability in SPE.

In this work, Molecular Dynamic (MD) simulations are employed in order to probe the system at the nanoscale. To form micro-separated morphologies with well-defined structures, χN should exceed that of the order-disorder-transition (ODT), which is only attained in high molecular weight DBP. In principle, atomistically-detailed DBP models could be employed such as in the recent study of doped DBP systems by Sethuraman et al. [18]. However, while static thermodynamic properties of polymeric materials at the atomistic scale can be obtained from short simulations ($2ns$) with reasonable accuracy [18], calculation of transport and dynamic properties typically require much longer simulations to cover the time scales associated with different relaxation processes of the melt ($\gg 10ns$) [19]. In our study, for computational efficiency, polymers were described using a coarse-grained representation similar to the one used by Ganesan et al. [10] in their Kinetic Monte Carlo study of ions diffusion in Lamellae-forming DBP, and the model used by Seo et al. [20] for the diffusion of selective penetrants in tapered Lamellae-forming block copolymers.

2.3 Methodology

The well-known bead-spring model of Kremer and Grest (K-G) [21] was adopted as it has been widely used to study dynamic [22], rheological [23, 24], and mechanical properties [25–27] of homopolymer and polymer networks, and to investigate DBP self-assembly [28, 29]. This model has been shown to reproduce the qualitative behavior of the self-diffusion coefficient [21], and shear viscosity [23] of polymer chains as a function of N, both in the Rouse and reptation regimes, suggesting that it should be suitable for the purpose of this work under some assumptions.

The force field parameters were obtained from a study that was concerned with mapping the reduced temperature (T^*) to χN utilizing a modified K-G Model that is applicable for DBPs [28]. The force field consists of a shifted Lennard Jones (LJ) non-bonded interaction for like polymer species, and a purely repulsive Weeks-Chandler-Andersen (WCA) for unlike species (eq. 2.1), where ϵ_{ij}, σ_{ij}, r_{ij}, and $r_{c_{ij}}$ are the interaction energy, effective diameter, separating distance, and the potential cut-off for the interaction between particles i and j, respectively. The bonded interactions are represented by the Finitely Extensible Nonlinear Elastic (FENE) potential that does not allow for beads overlap (eq. 2.2), where K is the spring constant, and R_0 is the maximum allowable bond length. Electrostatic interactions are not included explicitly due to the effective screening discussed in Appendix A.

$$U^{(LJ/WCA)}(r_{ij}) = \begin{cases} 4\epsilon_{ij}\left[\left(\frac{\sigma_{ij}}{r_{ij}}\right)^{12} - \left(\frac{\sigma_{ij}}{r_{ij}}\right)^{6} - \left(\frac{\sigma_{ij}}{r_{c_{ij}}}\right)^{12} + \left(\frac{\sigma_{ij}}{r_{c_{ij}}}\right)^{6}\right] & r < r_{c_{ij}} \\ 0 & r \geq r_{c_{ij}} \end{cases} \tag{2.1}$$

$$U^{FENE}(r_{ij}) = -\frac{1}{2}KR_0^2 \ln\left[1 - \left(\frac{r_{ij}}{R_0}\right)^2\right] + 4\epsilon_{ij}\left[\left(\frac{\sigma_{ij}}{r_{ij}}\right)^{12} - \left(\frac{\sigma_{ij}}{r_{ij}}\right)^{6}\right] + \epsilon_{ij} \tag{2.2}$$

To account for polymer-ion interactions, the force field from Ref. [28] was augmented with parameters that approximately account for such interactions. Assuming that one LJ bead represents a Kuhn length (l_k) of the polymer (e.g., PEO having $l_k = 0.8nm$ [30]), and since the radius of lithium, for instance, is $0.18nm$ [31], a DBP monomer is represented by a LJ bead twice larger in diameter and ten times heavier than the ion bead (C). The polymer-ion interaction was assumed to be describable by a LJ potential energy function and calibrated in a Lamellae (L) morphology (i.e., symmetric volume fractions of the constitutive

Table 2.1: The force field interactions parameters.

Interaction Type	LJ			FENE	
	ϵ_{ij} (ϵ)	σ_{ij} (σ)	r_c (σ)	R_0 (σ)	K (ϵ/σ^2)
A-A (B-B) [28]	1.0	1.00	2.5[a]	1.5	30
A-B [28]	1.0	1.00	$2.0^{1/6}$[b]	1.5	30
A′-A′	1.0	1.00	2.5[a]	1.5	30
A-A′	1.0	1.00	$2.0^{1/6}$[b]	1.5	30
A′-B	1.0	1.00	$2.0^{1/6}$[b]		
C-C	1.0	0.50	$2.0^{1/6}$[c]		
A-C (A′-C)	4.0	0.75	2.5[a]		
B-C	2.0	0.75	$2.0^{1/6}$[b]		

[a] Long range attractive interaction included in the potential; [b] WCA due to incompatibility; [c] WCA to mimic the dilute concentration limit.

blocks) due to the ease of characterizing the ions distributions in the polymer and the readily available data in the literature [5]. The ions (C) were effectively trapped in the conductive domain (as in real systems [5]) for $\epsilon_{AC} = 4.0\epsilon$, where A is the conductive domain, as shown in Appendix B. The complete list of the force field parameters is shown in Table 2.1.

Given the degree of coarse graining in our model (i.e., $\sim$ 3 PEO monomers per LJ bead based on a PEO monomer size $\approx$ $0.28nm$ [32]), short-time (sub-diffusive) dynamics associated with atomistic details of intrachain diffusion and C coordination are not captured explicitly. However, the long-time diffusive process dominated by interchain hopping [19] is captured well, which in our systems is attained at a very short time as shown in the time-dependence of ion

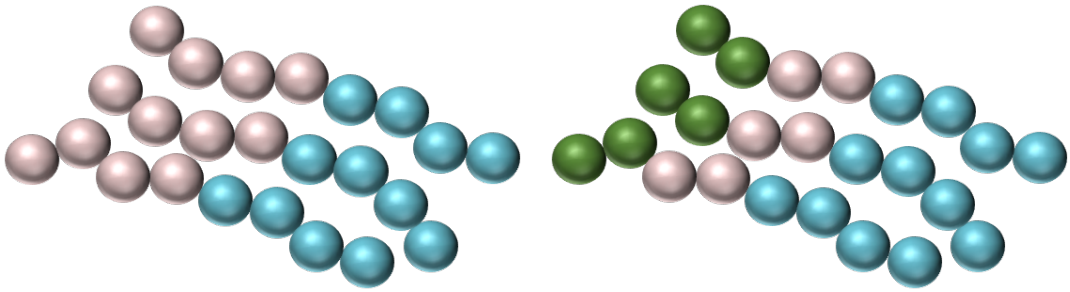

(a) (b)

Figure 2.1: (a) DBP with A-b-B architecture and (b) TBP with A'-b-A-b-B architecture, where A' is represented by the green beads, A by the pink beads, and B by the cyan beads.

displacement (Δx) in the direction of applied external force (F) in Appendix C. As a result, the model is representative of the ionic transport when the diffusion is dominated by the interchain hopping mechanism [19]. Note also that ion coordination is expected to be less prevalent in microphase separated DBP regions exhibiting stretched chain conformations [33].

Two polymers architectures were considered in this study: (1) the typical DBP with A-b-B architecture, where A is the conductive domain, and B is the non-conductive domain, and (2) a triblock terpolymer (TBP) with A'-b-A-b-B architecture, where A and A' are conductive, and B is non-conductive (Figure 2.1). The different blocks are incompatible to each other which drives the phase segregation.

All the simulations were conducted using the Large-scale Atomic/Molecular Massively Parallel Simulator (LAMMPS) [34]. The equilibrated structures were obtained from initially random configurations using a canonical ensemble (NVT), except if otherwise specified. The equations of motions are integrated with a time step of $\delta t = 0.001\tau$ using a Velocity-Verlet algorithm. T was set to

2.6 ϵ/k_B corresponding to $\chi N \approx 20$ for the shortest chain length ($N = 10$) [28] and controlled using the Nosé–Hoover thermostat (a thermostat that is suitable for studying dynamic and transport properties due to its deterministic nature [35]). A damping parameter of 0.5 τ was used, which for our system provides a comparable diffusion coefficient to that obtained from the microcanonical ensemble (NVE) in agreement with previously published study [35]. ρ of the polymer was kept at $0.85\sigma^{-3}$, a value typically used for coarse grained homopolymer [22, 23, 36], and DBP systems [24, 28, 37–39]. An underlying assumption for using a fixed ρ for different N is that ρ becomes largely independent of molecular weight at relatively small molecular weight (i.e., for dilute free-end groups) as has been observed in experiments [40], atomistic simulations of PEO [41] and K-G model for the L morphology over the same range of chain lengths used here [37, 38]. Pressure isotropy was monitored to ensure the box dimensions are appropriate to accommodate the natural domain spacing of the different morphologies [42]. The isothermal-isobaric ensemble (NPT) was used for the triblock terpolymer (TBP) system (A'-b-A-b-B) to match the pressure of the DBP systems, because otherwise keeping the same volume would lead to a significant compression of the B domain. The pressure damping parameter for the Nosé–Hoover barostat was set to 5.0 τ.

The TBP systems were obtained from the equilibrated L phase system for $N = 40$ by changing the type of a certain number of beads starting from the end-group of the A block to systematically delineate the effect of the A′ fraction (ψ) on μ, where $\psi = N_{A'}/(N_{A'}+N_A)$.

The different morphologies of DBP (L, Gyroid (G), and Hexagonal Cylinder (HC)) were obtained by varying the of the constitutive blocks (ϕ_1) for different

N at a constant T (Table 2.2). All the DBPs were obtained from a random initial configuration that was allowed to evolve and reach its equilibrated structure (i.e., constant temperature, energy, and pressure), except for the G phase whose initial configuration was an equilibrated structure from a previous Dissipative Particles Dynamic (DPD) study by our group [43]. The use of this equilibrated structure is justified because we are only interested on the thermodynamic equilibrium properties of the structure, which are independent of the initial configuration. Moreover, the system was allowed to expand to the desired density in the new force-field, and the morphology, in all cases, was confirmed by computing the structure factor ($S(\boldsymbol{q})$):

$$S(\boldsymbol{q}) = \frac{\left(\sum_j \cos\left(\boldsymbol{q}.\boldsymbol{r}_j\right)\right)^2 + \left(\sum_j \sin\left(\boldsymbol{q}.\boldsymbol{r}_j\right)\right)^2}{n} \tag{2.3}$$

where $\boldsymbol{q}$ is the wave vector (restricted to integer values of the wavelength), $\boldsymbol{r}_j$ is the position vector of bead j, and n is the total number of beads used in the calculation.

Ionic mobility simulations were performed by applying a small external force ($F = 1.0\ \epsilon/\sigma$), which yields a linear response behavior (Appendix D), to drive the ions in the direction parallel to the interface (for L and Hexagonal Cylinder (HC) morphologies) or perpendicular to the interface (for HC morphology), which mimics the electric field in experimental and all-atom computational studies [44]. After the external force is applied, the ions were allowed to equilibrate before a production run is performed to get μ through Ohm's law:

$$\mu = \frac{\langle v \rangle_i}{F} \tag{2.4}$$

where $\langle v \rangle_i$ is the drift velocity ensemble average obtained from the average distance traveled by all ions at a given time t in the direction of the applied force

Table 2.2: DBP simulated morphologies and their corresponding ϕ_1 for a given N.

N	ϕ_1		
	L	HC	G
10	0.50	-	-
14	0.50	0.21	-
18	-	-	0.33
24	0.50	0.25	-
40	0.50	0.25	-
60	-	0.25	-
64	0.50	-	-
76	0.50	-	-
Initial Structure	Random	Random	DPD Structure

(Δx_i). To reduce the statistical uncertainty in Δx_i, each configuration is treated as a time origin (t_0), and Δx_i values are averaged over t_0:

$$\Delta x_i = \lim_{t \to \infty} \langle x(t + t_0) - x(t_0) \rangle_{t_0} \tag{2.5}$$

A linear regression fit of Δx_i versus t is used to obtain (v_i).

2.4 Results and Discussion

At the beginning, the model was tested by reproducing the qualitative dependence of μ on the DBP N, with L morphology, from previous published studies [5, 9–11] by adding C at a fixed low concentration (< 0.002 C/A by volume) to mimic systems in the dilute concentration regime, where ion-ion interactions

are minimal and complete salt solvation is approached [45,46].

μ was found to increase with N at different T as shown in Figure 2.2, in qualitative agreement with experimental [5,9,33] and computational findings [10]. Nevertheless, counter to experimental findings, our results show a small dependence of μ on N, suggesting that grain boundaries, present in experiments, likely influence μ in polymer electrolytes. It is also illustrated in Figure 2.2 that the increase in μ is more pronounced for higher T and when the B domain is frozen. In Florys theory, unlike particle contacts in isotropic "well-mixed" polymer mixtures are quantified by the coordination number [47]. Similarly, we used the coordination number to quantify the extent of microdomains mixing (β) by integrating the A/B radial distribution function ($g_{AB}(r)$), around a central atom A, up to the first minimum in $g_{AB}(r)$ (r_m):

$$\beta = 4\pi \int_0^{r_m} r^2 g_{AB}(r) \rho dr \tag{2.6}$$

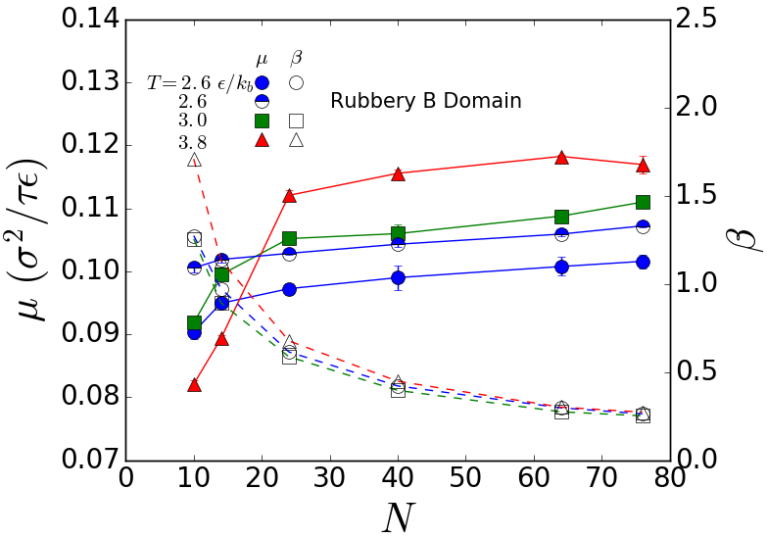

Figure 2.2: The impact of N and T on μ and the extent of microdomains mixing (β) as captured by the coordination number of A-B, where A is the central atom.

As shown in Figure 2.2, β decreases while μ increases with N for all T. Ganesan et al. [10] were the first to identify that the reduction of the fraction of ions mixing with the interface of the two blocks is related to the increasing trend of μ with N. The main advantage of our definition is that it provides a more intuitive framework to understand the effect of T on β as it accounts for the segregation of the blocks rather than that between the ions and the non-conductive domain. Interestingly, the dependence of β on N, at a constant T, using both methods is qualitatively similar due to the fact that C is trapped in the conductive domain (i.e., ions probe the same environment as the conductive domain experiences).

The effect of T on μ is most significant for small N, which is also reflected on the interfacial fluctuations of the lamellae structure as shown in Figure 2.3. Macroscopically however, the structure for all systems retains some degree of order as captured by the presence of a primary peak in the structure factor ($S(\boldsymbol{q})$) in Figure 2.3a.

When χN approaches the ODT, the effect of the interfacial fluctuations becomes more dominant, resulting in a reduced μ value as seen for $N = 10$ and 14 at $T = 3.8\ \epsilon/k_b$. In other words, C experience the interfacial fluctuations as structural defects that hinder their motion, which illustrates the importance of a percolated straight pathway for the transport of C (and to some extent the detrimental effect of grain boundaries). As β reduces, so does the probability of C to encounter the glassy and energetically unfavorable environment of B.

By virtue of phase separation, spatial ρ variations are created within the polymer matrix as shown in Figure 2.4, whose magnitude agrees with the predictions of polymer Density Functional Theory (DFT) for a lamellar-forming DBP [48]. There are several factors that influence the homogeneity of the local

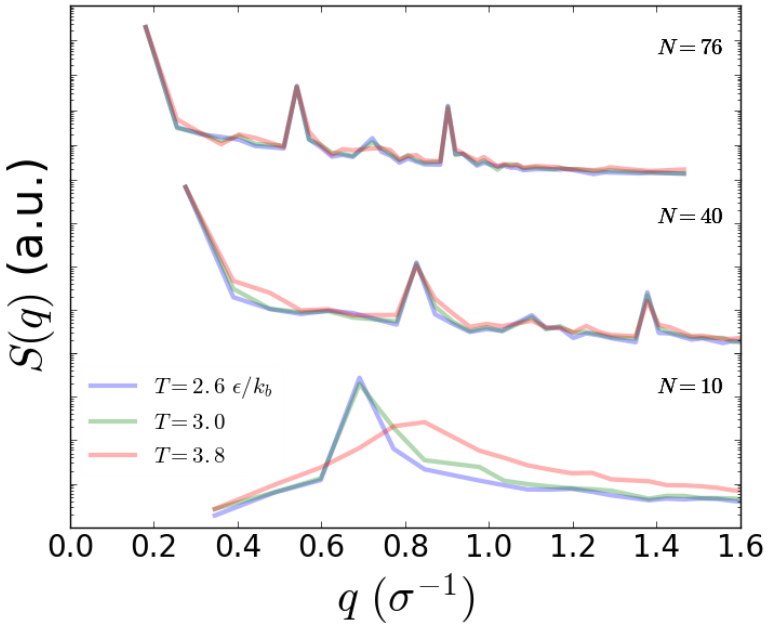

(a)

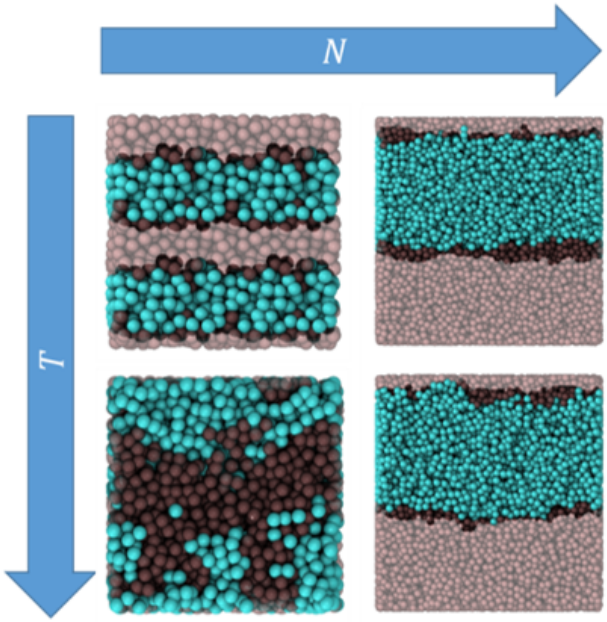

(b)

Figure 2.3: Effect of N and T on (a) $S(q)$, where the smallest q is within one-half of the simulation box dimensions, and (b) structure of the Lamellae, where the A-domain beads are in pink and the B-domain beads are in cyan and shade is in the darker color. Visuals are generated using Visual Molecular Dynamics (VMD) package [2].

ρ in polymers. First, the free-end groups, which tend to localize in the center of the domain, result in a slight decrease in the local ρ due to efficient packing. Another factor that influences the local ρ is the presence of interfaces arising from the chemical incompatibility. Despite the small size of C relative to the polymer segments, ρ of the polymer influences μ significantly as shown in Appendix E for two sizes of C (σ_{cc} = 0.25σ and 0.50σ). Expectedly, the effect of global ρ on μ is slightly reduced for the smaller ion.

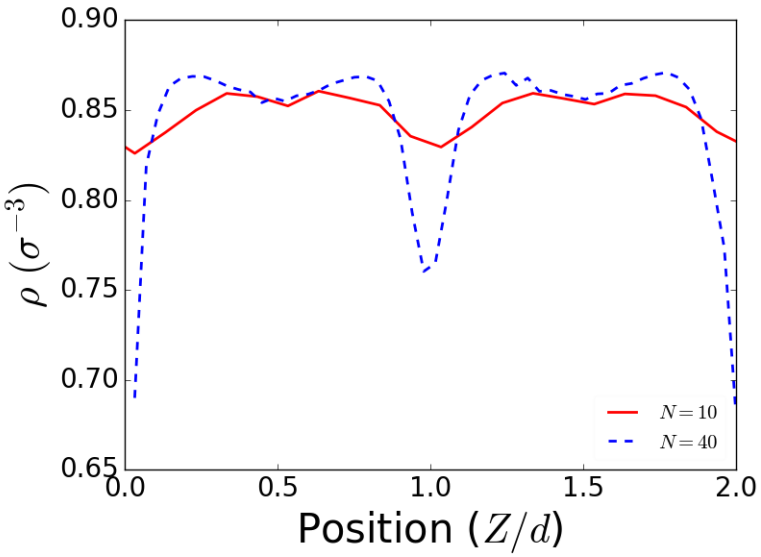

Figure 2.4: The impact of N on the ρ profile of the polymer in the direction perpendicular to the Lamellae interface (Z) at $T = 2.6\epsilon/k_b$. Position = 0.0, 1.0, and 2.0 correspond to the interface between the two blocks.

To illustrate the effect of the presence of interfaces on μ, we studied the TBP system depicted in Figure 2.1a. In this system, the B domain was set to be above its T_g. By varying ψ, the frequency and magnitude of ρ-depleted regions are altered (see Figure 2.5a), which result in an improved μ at the two temperature we tested (Figure 2.5b). A similar effect is seen for different N. However, non-monotonic behavior may occur due to the formation of perforated L where the B domain penetrates the A domain significantly, hindering ionic mobility. The

dependence of μ on the local ρ indicates that for the conditions probed, μ is independent of the macroscopic viscosity (i.e., segmental motion) and rather depends solely on the local environment since, otherwise, the mobility would reduce due to the reduced mobility of segments proximal to the interfacial zone [49]. This is true since drag from the polymer is negligible for the small and light ions we used, whose relaxation time is faster than that of the polymer segments. Similar results were seen for attractive nanoparticles diffusing in a polymer melt [22, 50]. Our results suggest that local ρ variations can be exploited as a design criteria for improving μ. Note also that our TBP should also enhance mechanical stability due to a concomitant increase in the order (number of layers) in the system.

By varying the DBC morphology, the A domain thickness and contour length change, which impact both β and the tortuosity (λ). To examine these effects, we prepared systems of different morphologies that are typically used in electrolyte systems for various N (See Table 2.2). As shown in Figure 2.6a, μ varies significantly by changing the morphology, and the direction of applied field, even for the same N (Figure 2.6b). Nonetheless, the general trend of increasing μ with N holds for all morphologies because of the reduction in β.

To analyze the results, we plot in Figure 2.7a correlation of β (calculated via eq. 2.6) and χN for the different morphologies. The correlation indicates that regardless of the morphology, χN depends on β following approximately the same scaling. Our definition of β accounts for the fraction of A beads in close proximity to the B domain. Thus, β is a function of χN (i.e., segregation strength) and the number of A beads (N_A), which allows β to be interpreted as the ratio of the interfacial zone thickness (Δ^*) to the conductive domain thickness (d).

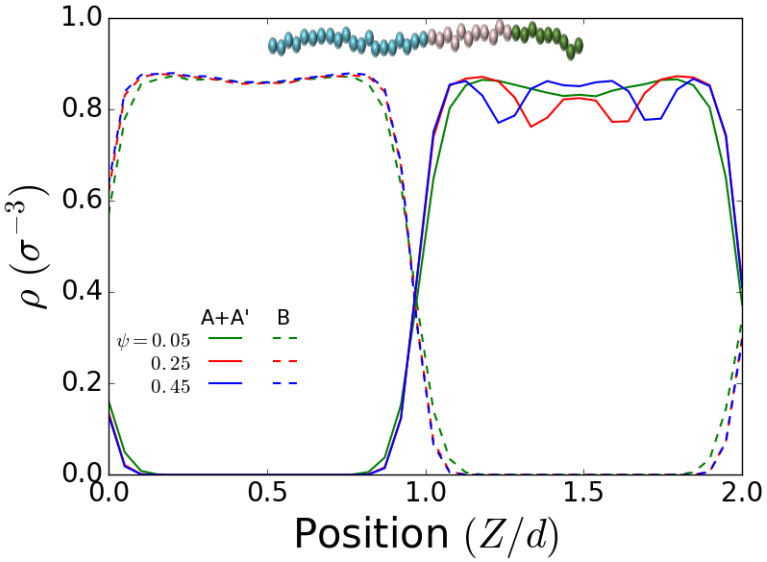

(a)

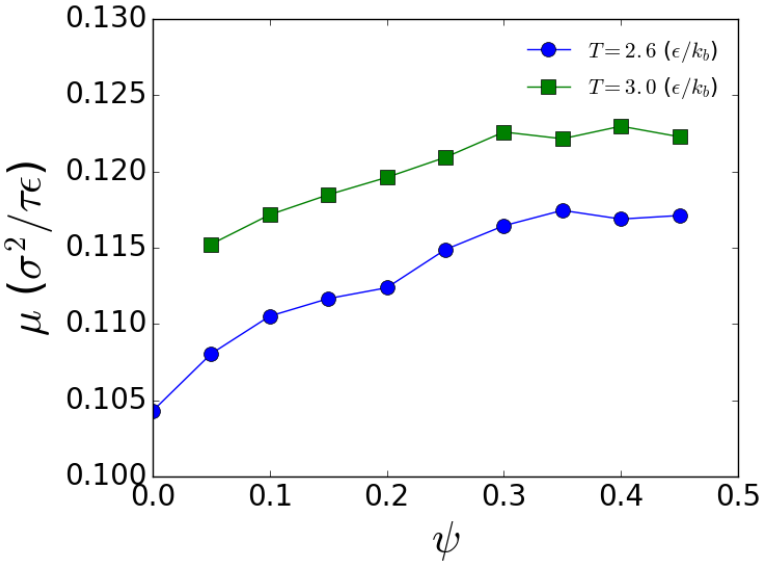

(b)

Figure 2.5: The effect pf ψ on (a) the ρ profile of the conductive domain (A+A'), and B in the direction perpendicular to the Lamellae interface (Z), where each domain has a thickness $\approx d$, at $T = 2.63\ \epsilon/k_b$ (A depiction of the TBP sysyem with $\psi = 0.45$ appears in the inset for $N = 40$) and (b) on μ for $N = 40$ at $T = 2.63\ \epsilon/k_b$ and $3.0\ \epsilon/k_b$.

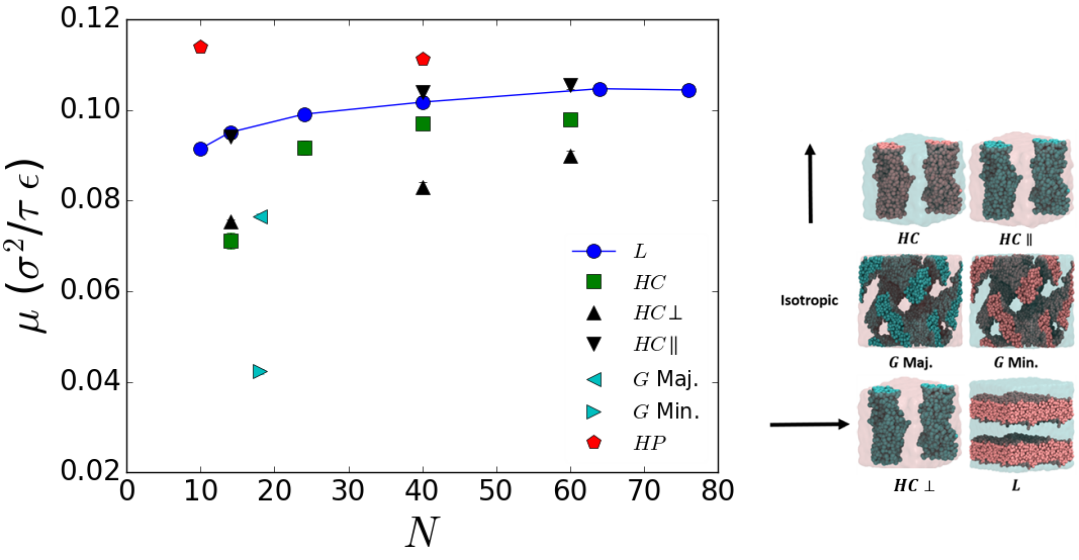

(a) (b)

Figure 2.6: (a) Effect of N, morphology, and the direction of applied force on μ at $T = 2.63\ \epsilon/k_b$. (b) Depiction of the phases used in the legend of (a), where the arrows represent the directions of the applied force, and the pink and cyan colors represent the conductive and non-conductive domain, respectively.

Semenov developed a theoretical description of how Δ^* and d depend on χ, N, and χN for L morphology [51]:

$$\Delta^* = \left[\Delta^2 + \frac{v\Delta_0}{2a^2}\ln\frac{d}{\Delta_0}\right] \tag{2.7}$$

$$d = 2(3/\pi^2)^{1/3} a N^{2/3} \chi^{1/6} \tag{2.8}$$

, where $\Delta = \Delta_0\left[1 + \frac{1.34}{(\chi N)^{1/3}}\right]$, $\Delta_0 = 2a\chi^{-1/2}$, v is the volume of a polymer segments (i.e., polymer bead in our model), and a is the segment length. The dependence of Δ^* on N of our systems is similar to that obtained from the theoretical relation for temperatures approaching the strong-segregation regime (Appendix F). Moreover, as seen in Figure 2.7, β and Δ^*/d have the same scaling with χN providing a theoretical basis to the simulation trends.

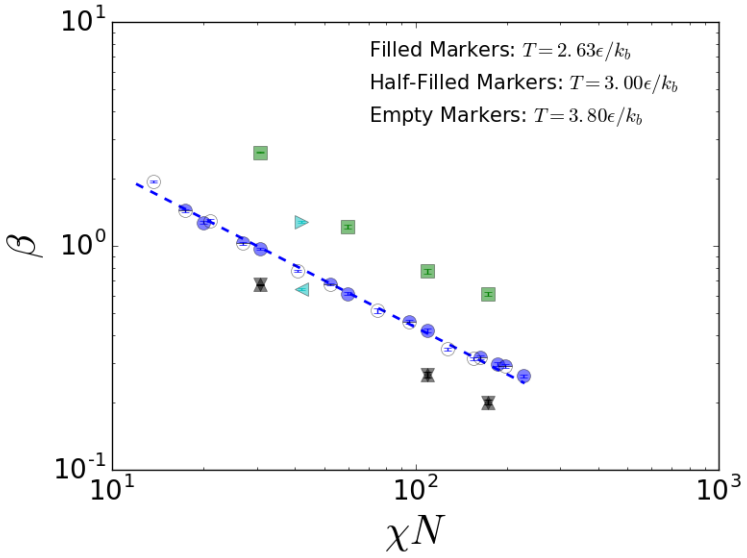

Figure 2.7: The effect of χN and morphology on β. The dashed blue line is the scaling of Δ^*/d from eq. 2.7-2.8. The legend is the same as that for Figure 2.6a.

We expect that μ, which relates $\langle v \rangle_i$ to F (eq. 2.4), will depend inversely on λ, i.e., $\mu \sim \lambda^{-1}$, in analogy to how the permeability in pressure-driven fluid flow [52] and the effective diffusion coefficient [53] depend on tortuosity. From the geometric tortuosity definition (as the ratio of the average length of the possible geometric paths to the straight-line path length) [52], λ is unity for Lamellae (L), HC when the cylinder is conductive (HC), and HC when the continuous matrix is conductive and the applied field is parallel to the cylinders (HC $\|$). λ for the G phase where the minority component is conductive (G Min.) was found to be ≈ 2.04 from a geometric analysis of the structure [54]. For Hexagonal Cylinder when the continuous matrix is conductive and the force is applied perpendicular to the cylinder axes (HC $\perp$), λ was calculated based of the geometric tortuosity definition, which depends on domain size and cylinder diameter (see calculations in Appendix G.1). λ for HC $\perp$ was found to depend on N due to an increase in the spacing between cylinders hereby reducing λ. Since identify-

ing λ for the Gyroid when the majority component is conductive (G Maj.) from the geometry of the structure is non-trivial, λ was calculated based on biased diffusivities, in which the non-conductive domain is frozen and the structure of the G phase in absence of the conductive domain beads is probed (see details in Appendix G.2).

Since β depends on T, the effect of T on μ can be accounted for by the T dependence of μ for the homopolymer (HP) system [9] (Appendix H). We can account for this T effect and the tortuosity effect (i.e., on account that $\mu \sim \lambda^{-1}$) by defining a $T - \lambda$ corrected mobility (μ^*):

$$\mu^*(T_0) = \mu(T)\frac{\lambda}{\lambda_{HP}}\frac{\mu_{HP}(T_0)}{\mu_{HP}(T)} \tag{2.9}$$

, where T_0 is a reference temperature, and λ_{HP} is unity. As shown in Figure 2.8, the plots of μ *vs.* β for the various morphologies collapse into a single universal curve regardless of T, as long as it is sufficiently far from the ODT temperature. Indeed, the only two cases that exhibit pronounced deviations in Figure 2.8 correspond to $N = 10$ and 14 at $T = 3.8\epsilon/k_b$ in Figure 2.2-2.3, where the close proximity to the ODT temperature renders interfacial fluctuations dominant. The fitted line in Figure 2.8 approaches the homopolymer mobility (for $N = 40$) at $\beta = 0.0$, when μ becomes independent of the macroviscosity (i.e., segmental motion or α-relaxation) in homopolymer melts [50]. Note that one can use the correlations in Figure 2.7 to predict β for different phases and conditions and then use Figure 2.8 to predict μ. Since β depends on T, the effect of T on μ was accounted for from the T effect on μ for homopolymer system [9] (Appendix H).

Counter to experimental studies suggesting improved μ in continuous networks, our results indicate that μ is impaired by the tortuosity of the A domain at the nano-scale (i.e., for perfect morphological monodomains). In exper-

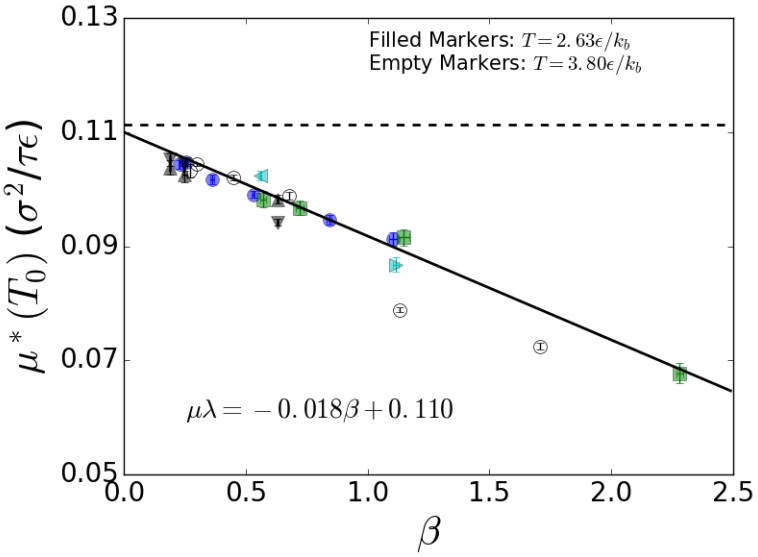

Figure 2.8: Effect of β on $\mu^*(T_0)$ (eq. 2.9), where $T_0 = 2.63\epsilon/k_b$. The black solid line is a fit to the *HC* data (green squares), and the dashed line is the $\mu_{HP}(2.63\epsilon/k_b)$ for $N = 40$. The non-conductive domain is frozen in all systems. The symbols are the same as in Figure 2.6a.

imentally realizable systems, however, continuous morphologies may still be appealing for ionic conduction because they are expected to experience minimal effect from the misalignment of grain boundaries compared to other morphologies [13], due to the high probability of continuity of the domains across grain boundaries.

2.5 Conclusions

In summary, we have implemented a coarse-grained MD model for studying the transport of ions under an external driving force in diblock copolymers that form Lamellae, Hexagonal Cylinder, and Gyroid morphologies by varying the volume fraction of the minority block. In qualitative agreement with previ-

ously published computational and experimental studies for Lamellae phases, the model can predict the increasing trend in ionic mobility with chain length. As chain length and conductive domain thickness increase, so does the probability of ions residing away from the interfacial region.

The beneficial effect on ionic mobility of local density depletion regions in a Lamellae forming diblock copolymer was exploited by introducing additional interfaces within the conductive domain, which resulted in improved ionic mobility.

In contrast to experimental studies that show an advantage of 3D interconnected conductive domain, our results suggest that the increased tortuosity of such a domain tends to reduce ionic mobility. The tortuosity effect was studied by varying the morphology, utilizing the different blocks as being conductive, and by applying external force in different directions relative to the inter-face (i.e., in Hexagonal Cylinder when the majority block is conductive). Most likely, the discrepancy in the results arises from the structural defects present in experimental systems. In the future, we plan on addressing the effect of specific types of defects on the ionic transport in diblock copolymer systems of various morphologies, an undertaking that was beyond the scope of this work.

Importantly, after accounting for microdomains mixing and the tortuosity of the conductive domain, a single universal correlation is obtained for the ionic mobility for different morphologies, chain lengths, and temperatures indicating that ionic mobility, in the nano-scale, is mainly controlled by the two microstructural factors.

CHAPTER 3

CORRELATIONS BETWEEN MORPHOLOGY AND ANISOTROPIC TRANSPORT PROPERTIES OF DIBLOCK COPOLYMERS

3.1 Abstract

Molecular simulations of coarse-grained diblock copolymers (DBP) were conducted to unveil correlations between morphology and transport properties. It was found that in the strong segregation limit (i.e., high χN, where χ is Flory-Huggins parameter and N is degree of polymerization), the presence of the DBP interfaces imposes topological constraints similar to those of entanglements as manifested in the rheological signature of the polymer (i.e., relaxation time and plateau modulus). Furthermore, compared to the behavior of isotropic melts, the crossover from Rouse to reptation scaling of the self-diffusion coefficient (D) parallel to the DBP interface takes place at a smaller N, an effect that depends on temperature and is more pronounced in the Lamellae morphology than in the Hexagonal Cylinder morphology. Additionally, it is shown that for an entangled melt (i.e., $N > N_e$ where N_e is the entanglement length) block retraction is instrumental for chains to diffuse parallel to the interface between lamellar layers. Lastly, it is found that the anisotropic viscosity of the different morphologies is mostly affected by the orientation of the chains relative to the shear flow direction, exhibiting reduced values when chains align in the neutral or flow directions.

3.2 Introduction

In microphase separated morphologies of diblock copolymers (DBP), naturally conflicting properties are able to exist in nanoscale proximity, which makes these materials attractive for applications ranging from lithography to artificial organ technology, drug delivery, and energy storage [3,8]. For example, the mechanical stability of solid polymer electrolytes used in battery applications is essential for sustainable and safe operations [4]. DBPs have been thoroughly studied as a potential materials platform to improve electrolyte stability and safety [5–7]. While the conductive block is typically flexible and contains polar sites that can solvate salts, the other non-polar block can be made rigid or glassy to impart the system with the mechanical stability needed to suppress dendrite formation. In drug delivery applications, blocks with different hydrophobicity can be utilized in order to transport hydrophobic drugs in the bloodstream at concentrations above their intrinsic water solubility limit. The hydrophilic block forms a protective shell against bio-degradation of the bioactive molecules enhancing the drug integrity and performance. Additionally, the reversible nature of the temperature-driven DBPs ordering (i.e., from order to disorder and vice versa) allows for thermally controlled release of the bioactive molecules [8]. Hence, characterizing viscoelastic and dynamic properties which directly correlate with mechanical stability and ordering kinetics of DBPs, is of critical importance from both fundamental and application perspectives. Furthermore, studying model DBP systems of linear chains could provide insights relevant to other more complex DBP resembling systems, such as polymer-grafted nanoparticles, polymer brushes [55], and protein lipid bilayers.

In the past few decades, theoreticians and experimentalists have devoted

much attention to understanding the dynamic and viscoelastic properties of homopolymers melts, and their departure from those of small organic liquids. One important parameter that largely influences the viscoelastic behavior of polymer melts is the degree of polymerization (N). The dependence of the self-diffusion coefficient (D) with N in homopolymer melts follows a $N^{-\xi}$ scaling, where ξ is 1 in the Rouse regime (consistent with the Einstein Diffusion model), and 2 in the reptation regime (consistent with de Gennes' tube model), while the zero-shear viscosity (η_0) follows a N^{ξ} scaling, where ξ is 1 in the Rouse regime, and 3.4 in the reptation regime [56]. In the Rouse regime (i.e., $N < N_e$), the polymer chains can slide past one-another. Such diffusion mechanism does not take place when $N > 2N_e$ due to the constraints imposed by the melt that confine a particular chain to a tube whose diameter (d_T) can be correlated with the end-to-end distance of a chain with N_e segments (i.e., $d_T \approx aN_e^{1/2}$, where a is the Kuhn length) [57]. Entanglements only allow for diffusion along the contour of the tube, whose length is L_0, within which the chain-end 'reptates' from one tube to the next following the path taken by other segments of the chain. Within a tube, the polymer segments locally diffuse following the Rouse model; however, for the whole chain to diffuse it needs to travel a distance L_0 equivalent to its end-to-end distance (R_{ee}), thereby increasing the relaxation time of the chain and giving rise to the reptation scaling regime. The theoretical scaling predictions in the Rouse and reptation regimes for both D and η_0 were found to explain experimental and computational results for homopolymer melts with only a slight difference in the ξ observed in the reptation regime [21,23,58]. The D scaling with N is more sensitive to entanglements than that of η_0 since the Rouse contribution to η_0 is strong and it is only at $N \gg N_e$ that the exponential component, arising from entanglement, becomes dominant [23].

While the dependence of dynamic and viscoelastic properties on a wide spectrum of parameters (i.e., temperature, concentration, and chain length), and polymer designs (e.g., branching) is well understood for homopolymer melt systems [59–63], it is less so for DBP systems. Depending on the volume fraction of the minority block (ϕ_1), and the segregation strength (χN, where χ is the Flory-Huggins parameter), linear A-b-B DBPs form various micro-segregated structures below the order-disorder temperature (T_{ODT}). The introduction of interfaces due to the chemical incompatibility of the constituent blocks gives rise to additional energetic and entropic barriers that influence the transport and viscoelastic properties of DBPs.

It was previously suggested that in the entangled regime, strongly segregated DBPs (i.e., for $\chi N \gg (\chi N)_{\mathrm{ODT}}$, where $(\chi N)_{\mathrm{ODT}}$ is the χN at the order-disorder transition) with Lamellae (L) morphology (i.e., $\phi_1 = 0.5$) diffuses parallel to the interface by a block retraction mechanism (i.e., one block retracts to the interface before the lateral diffusion along the interface can take place) [64,65]. However, this block retraction mechanism was not observed in the simulation study of Murat et al. [37,38], who argued that Lamellae-forming DBPs have reduced entanglement density compared to homopolymers due to the increased ordering in the system. Using Kinetic Monte Carlo simulations, Pan et al. [66] examined DBPs with L morphology and found, by comparing D for a wide range of N at a fixed low χN, that the crossover N from Rouse to repation scaling (N_c) for DBPs is the same as that for the homopolymer. Most recently, Sethuraman et al. [67] and Ramirez-Hernandez et al. [68] used topological analysis to identify local distribution and global average entanglements in lamellae-forming DBPs. They found that N_e in DBPs ($\approx$ 40) is slightly lower than in homopolymers ($\approx$ 44) [68]. While the dynamic properties of DBPs have been

the subject of several experimental studies, it is very difficult to deconvolute the anisotropic diffusion tensor components arising from the spatial orientation of the interfaces, due to both the presence of multiple grain orientations seeded during phase microsegregation, and the different block chemistries used which potentially have different N_e [54, 65].

The stability of DBP phases under steady and dynamic oscillatory shear had been the subject of several studies [69, 70]. Depending on the shear rate and shear orientation (Figure 3.1), the DBP may exhibit transitions to different orientational states and to the disordered state. The dependence of the anisotropic viscosity tensor components on morphology has only been investigated in a few computational studies [71, 72]. Using steady-shear Dissipative Particle Dynamics (DPD) simulations, Zhang et al. [71] found that the zero-shear viscosity ($\eta_{0_{\alpha\beta}}$, where α is the flow and β is the velocity gradient directions) of the L phase, when flow and velocity gradient are parallel to interface ($L\,\|$), is lower than that of the Hexagonal Cylinder (HC), when flow is along the cylinder axis ($HC\,\|$). Ryu et al. [72] used linear response theory to calculate $\eta_{0_{\alpha\beta}}$ for the L morphology from the stress auto-correlation function. However, they combined the transverse ($L\mathcal{T}$) and perpendicular ($L\,\perp$) contributions into one component, despite these being fundamentally different due to the asymmetry of the structure [70]. Dynamic oscillatory shear experiments revealed that cubic DBP morphologies, such as the Gyroid (G) and Sphere (S) phases, exhibit a modulus plateau (G^0_{cubic}) for $N < N_e$ at a frequency smaller than the rubbery plateau (G^0_N), reminiscent of the effect of entanglements. G^0_{cubic} of the G phase was found to span several decades in frequency at the terminal regime (approaching the zero-shear limit). Moreover, it was found that randomly oriented L and HC phases exhibit a behavior intermediate between those of cubic phases and isotropic melts [73].

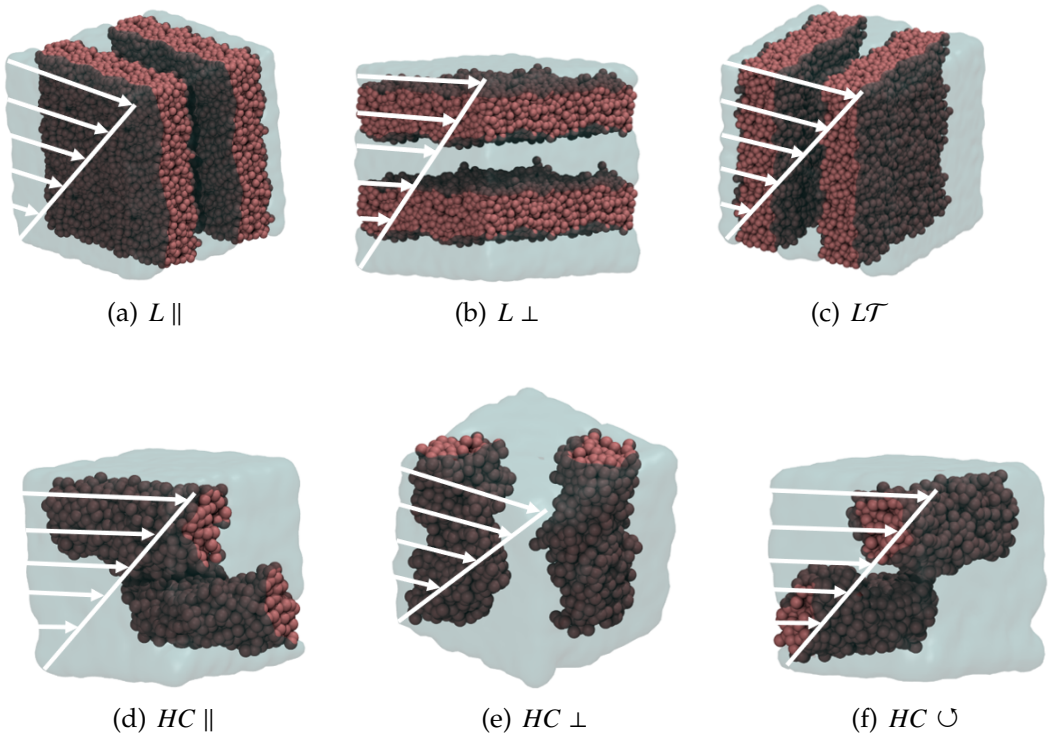

(a) $L \parallel$ (b) $L \perp$ (c) $L\mathcal{T}$

(d) $HC \parallel$ (e) $HC \perp$ (f) $HC \circlearrowleft$

Figure 3.1: Illustration of the different shear orientations possible for Lamellae (L) morphology (a-c) and Hexagonal Cylinder (HC) (d-f). Beads from only the minority block are displayed for clarity.

In this chapter, we study the effect of N and morphology on both the molecular diffusion and viscoelastic properties utilizing a coarse grained Molecular Dynamics (MD) method. The use of MD and model morphologies allow us to study the physical mechanisms underlying the different transport phenomena in the absence of major structural defects (i.e., within single-grain uniform structures). To form microphase separated structures with well-defined morphologies, χN should exceed $(\chi N)_{\mathrm{ODT}}$, which is efficiently achieved using a coarse-grained representation of the polymers. Using such model, we were able to examine a wide range of segregation strengths and to probe the Rouse and reptation regimes. We find that, depending on temperature, the DBP behavior tran-

sitions from the Rouse regime to the reptation regime at a shorter N compared to isotropic melts, which we attribute to the topological constraint imposed by the interface between the two blocks that gives rise to an entanglement-like rheological signature (i.e., the onset of a plateau modulus). We also demonstrate the importance of block-retraction to activate the lateral diffusion process for $N \gg N_e$. Finally, we show that trends in $\eta_{0_{\alpha\beta}}$ are correlated with the propensity for chain alignment with respect to the flow direction.

3.3 Methodology

Molecular Dynamic (MD) simulations were employed to study dynamic and viscoelastic properties of DBPs with various morphologies and chain lengths. All simulations were performed using LAMMPS [34]. The coarse-grained model adopted consists of beads and springs similar to that of Kremer and Grest for homopolymer melts, but adapted to DBP systems. The bead-spring model has proven useful in studying viscoelastic, dynamic, and static properties of neat [21, 23, 74] and filled [22, 24] polymer melts. Additionally, the model was successfully extended to study the phase behavior of DBP melts [28, 29, 75], and the response of DBP networks to tensile deformation [25–27].

To induce phase separation, like species interact via an attractive 6-12 Lennard-Jones potential (i.e., includes the attractive potential, $r_c = 2.5\sigma$), while unlike species interact via a purely repulsive potential known as the Weeks-Chandler-Andersen (WCA) (i.e., $r_c = 2^{1/6}\sigma$) potential (eq. 2.1), where $\epsilon_{ij} = 1.0\epsilon$, and $\sigma_{ij} = 1.0\sigma$. Bonded beads interact via the Finite Extensible Nonlinear Elastic (FENE) potential (eq. 2.2), where $R_0 = 1.5\sigma$, and $K = 30\epsilon/\sigma^2$. Without loss

of generality, the scaling quantities of mass (m), length (σ), and energy (ϵ) are set to unity. Also, the simulation quantities of concern are scaled as follows: temperature $T^* = k_b T/\epsilon$, time $t^* = t(\epsilon/(m\sigma^2))^{1/2}$, and number density $\rho^* = \rho\sigma^3$. The simulations were carried out in the canonical ensemble (NVT) with an integration time step (δt) of 0.001τ using a Velocity-Verlet algorithm. T was controlled using the Nosé–Hoover thermostat, a suitable choice for studying transport properties due to its deterministic nature [35], with a damping parameter of 0.5τ. ρ was kept at $0.85\sigma^{-3}$, a value appropriate for polymer melts [21,23,28], assuming incompressibility of the polymer across different N and T. Pressure isotropy was monitored to ensure that the box dimensions were appropriate to fit the natural domain periodicity of the system.

The different DBP morphologies were realized by varying ϕ_1 (Table 3.1). The equilibration procedure is the same as explained in Section 2.3.

Equilibrium and non-equilibrium MD simulations of the systems were implemented to measure dynamic and viscoelastic properties, respectively. The diffusion coefficient for motions parallel to the interface between the two blocks ($D_{\parallel}$) was computed in the L and HC phases. For the Gyroid (G) and Homopolymer (HP), the isotropic diffusion coefficient (D_{iso}) was calculated. The diffusion coefficient (D) was found from the Mean Square Displacement ($\left\langle \Delta \boldsymbol{r}(t)^2 \right\rangle$) using the Einstein relation of (eq. 3.1), where $\left\langle \Delta \boldsymbol{r}(t)^2 \right\rangle$ is averaged over time origin (t_0), and b is the dimensionality of the space where motion is tracked (e.g. $b = 1$ for HC phase, 2 for L phase, and 3 for isotropic phases) [76]:

$$D = \frac{1}{2b} \frac{\mathrm{d}}{\mathrm{d}t} \left\langle (\boldsymbol{r}(t + t_0) - \boldsymbol{r}(t_0))^2 \right\rangle_{t_0} \tag{3.1}$$

D is computed when a linear relationship between $\left\langle \Delta \boldsymbol{r}(t)^2 \right\rangle$ and t develops, indicative of diffusive motion. The production period of the simulation ranged

Table 3.1: DBP simulated morphologies and their corresponding ϕ_1 and T_{ODT} (in units of ϵ/k_b) for a given N.

N	ϕ_1 (T_{ODT})			
	L	G	HC	S
10	0.50 (4.5)	-	-	-
14	0.50 (6.8)	-	-	-
18	-	0.33 (8.0)	-	-
24	0.50 (12.5)	-	0.25 (9.0)	-
32	0.50 (16.8)	-	-	-
40	0.50 (20.8)	-	0.25 (15.3)	0.10 (5.6)
50	0.50 (25.4)	-	-	-
60	-	-	0.25 (22.4)	-
64	0.50 (31.2)	-	-	-
76	0.50 (35.6)	-	0.25 (27.5)	-
Initial Structure	Random	DPD Structure	Random	Random

from $75,000$ to $100,000\tau$. For these calculations we only tracked the positions of the minority component bead connected to the majority component (i.e., the "interface bead"). Note that since we are only interested in the long-time diffusion, its value is largely independent on whether for the calculations we track the interfacial bead, the chain center-of-mass, or any other bead.

To compute η_0, G', and G'', non-equilibrium MD simulations were performed using the SLLOD equations of motion [77]. A combination of steady and dynamic oscillatory shear were used to compute the zero-shear anisotropic viscosity components ($\eta_{0_{\alpha\beta}}$) using eqs. 3.2 and 3.3 below, where $\sigma^*_{\alpha\beta}$ is the stress tensor component in the flow direction α that is normal to velocity gradient

direction β, $\dot{\gamma}_{\alpha\beta}$ is the strain rate, and ω is the oscillation frequency:

$$\eta_{0_{\alpha\beta}} = \lim_{\dot{\gamma}_{\alpha\beta}\to 0} \frac{\sigma^*_{\alpha\beta}}{\dot{\gamma}_{\alpha\beta}} \tag{3.2}$$

$$\eta_{0_{\alpha\beta}} = \lim_{\omega\to 0} \frac{\sqrt{G'^2_{\alpha\beta} + G''^2_{\alpha\beta}}}{\omega} \tag{3.3}$$

The loss ($G''_{\alpha\beta}$) and storage ($G'_{\alpha\beta}$) moduli were calculated using eqs. 3.4 and 3.5, where $\sigma^*_{0_{\alpha\beta}}$ is the stress amplitude, $\gamma_{0_{\alpha\beta}}$ is the strain amplitude, and δ is the phase lag. $\gamma_{0_{\alpha\beta}}$ in the dynamic oscillatory shear simulations was fixed to 10%, which ensures operating in the linear response regime where the Cox-Merz Rule applies (Appendix I) [78]. $\sigma^*_{0_{\alpha\beta}}$ and δ were obtained from the least-square fit of the sinusoidal function (eq. 3.6) to the simulation data.

$$G''_{\alpha\beta} = \frac{\sigma^*_{0_{\alpha\beta}}}{\gamma_{0_{\alpha\beta}}} \sin(\delta) \tag{3.4}$$

$$G'_{\alpha\beta} = \frac{\sigma^*_{0_{\alpha\beta}}}{\gamma_{0_{\alpha\beta}}} \cos(\delta) \tag{3.5}$$

$$\sigma^*_{\alpha\beta} = \sigma^*_{0_{\alpha\beta}} \sin(t\omega + \delta) \tag{3.6}$$

3.4 Results and Discussion

Figure 3.2 shows our results for D of DBPs with various morphologies and N (listed in Table 2.2) including results of D for the HP for comparison. One unexpected observation in Figure 3.2 is that long DBP chains (high-N regime) diffuse faster in the HC phase than in the L phase. This may be due to the curvature

of the interface in the *HC* phase which allows interfacial beads to partially experience the environment of non-interfacial beads, which have faster short-time dynamics [49]. In contrast, while the *L* phase interfacial beads are surrounded by other interfacial beads in the interface plane. Figure 3.2 also shows that the isotropic diffusion of the *G* phase is a factor of 2 slower than that of the *L* phase, a difference that is in agreement with experimental findings and is attributed to the tortuosity of the *G* structure [54]. The trends in Figure 3.2 also indicate that DBP with *L* morphology exhibits a transition from the Rouse regime to the reptation regime at N_c that is shorter than that for *HP*. It is known that the onset of the reptation scaling occurs when $N_c \approx 2N_e$, where N_e is the entanglement N of *HP*. The slightly higher entanglement density of the *L* phase compared to the isotropic melt [68] cannot account for such "early" crossover ($N_c \approx N_e$) suggesting that an alternative diffusion mechanism takes place in the *L* phase.

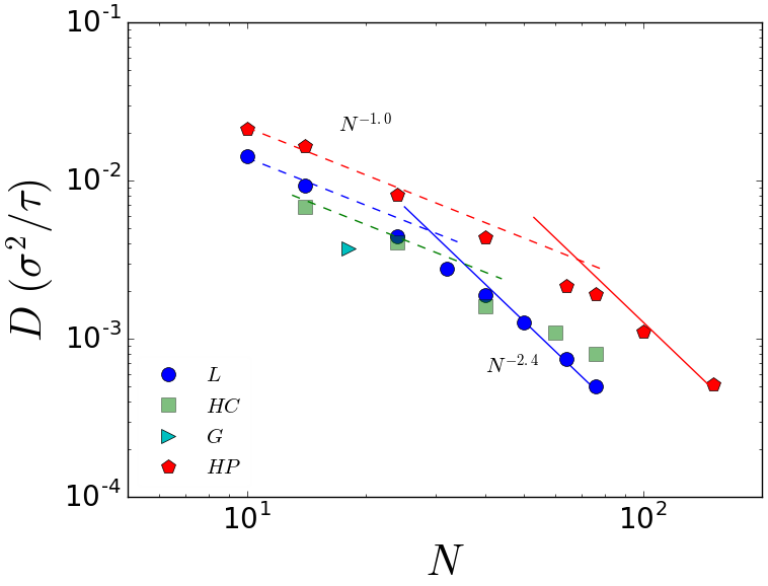

Figure 3.2: Effect of morphology and N on the interface-parallel D for *L* and *HC* phases, and the isotropic D for *G* phase and *HP* at $T = 2.6\epsilon/k_b$. The dashed (solid) line represent Rouse (reptation) scaling law.

Dalvi et al. [65] hypothesized that the lateral diffusion of an entangled L DBP melt proceeds via a block retraction mechanism, analogous to arm retraction in star polymers, where one block retracts to the interface in order for the chain to diffuse parallel to the interface plane. We tested this hypothesis by quantifying the effect on D by artificially reducing the tendency of block retraction. For this purpose, we pinned the end beads of either one or both blocks to a stiff harmonic spring potential: $\frac{1}{2}k(z_i - z_i^0)$ (with $k = 400\epsilon/\sigma^2$) to only restrict its motions in the direction normal to the interface (Z). The preferential position in the Z direction (z_i^0) for each of the affected end beads was taken to be its initial value in an equilibrated structure. Figure 3.3a shows the probability distribution of the center-of-mass position of one chain in the Z direction (COM_Z) when the pinning springs are or are not enacted. The COM_Z variance for the pinned system is $\approx 20\%$ of that for the free system. As shown in Figure 3.3b, for $N = 200$, the springs hinder the lateral motion significantly in both cases (whether one block or both blocks are pinned). As expected from the behavior of trapped entangled systems, $\left\langle \Delta r^2 \right\rangle_{\parallel}$ approaches a plateau value of $a^2 N_e$ (i.e., the squared diameter of the tube). On the other hand, for $N = 10$ (i.e., a non-entangled system), $\left\langle \Delta r^2 \right\rangle_{\parallel}$ is not effected by the springs (Figure 3.3c). Overall, these results indicate that for entangled chains, the cooperative motion of both blocks is required to activate the lateral diffusion process, further suggesting that the tubes formed by the entangled melt are preferentially aligned normal to the interface. Given that block retraction (taking place in the direction normal to the interface) is an essential component to the diffusion process of entangled self-segregated DBPs, we hypothesize that the pinning effect of the interface acts as a topological constraint akin to entanglements. In other words, the interface participates in the construction of the entanglement tube by preferentially aligning it in the direction

normal to the interface. This would hence explain the "early" crossover from Rouse to reptation scaling seen in Figure 3.2 for the L morphology ($N_c \approx 1N_e$) compared to HP ($N_c \approx 2N_e$).

To further test our hypothesis of the interface-$1N_e$ connection, we examine the effect of DBP segregation strength on N_c by varying T. Note that T is related to segregation strength in DBPs but has no effect on N_c for HP as shown in Figure 3.4 (which includes the simulation data from Bulacu et al. [79]). As shown in Figure 3.5a, N_c increases with T and, based on the interface-effect, it is expected that at $T \gg T_{\mathrm{ODT}}$, the behavior should approach that of HP. The effect of T on the segregation strength of the L phase can be captured by measuring the interfacial thickness (Δ^*), which is inversly related to χN [51], by fitting the order parameter $\psi(z)$ (eq. 3.7) to eq. 3.8, where $\phi_i(z)$ is the volume fraction of component i in the Z direction, and z_0 is the position at which $\phi_A(z) = \phi_B(z)$ [38]:

$$\psi(z) = \frac{\phi_A(z) - \phi_B(z)}{\phi_A(z) + \phi_B(z)} \tag{3.7}$$

$$\psi(z) = \tanh\frac{2(z - z_0)}{\Delta^*} \tag{3.8}$$

As shown in Figure 3.5b, Δ^* increases with T (for any N) until reaching a plateau value that is dependent on T. Since for the same T range, N_c is independent of T for HP, we attribute the change in N_c with T for DBPs to changes in the segregation strength as captured by the Δ^* trends in Figure 3.5b. The results from Figure 3.5b for $T = 2.63\epsilon/k_b$, where Δ^* is weakly dependent on N, indicate that $N_c \geq N_e$ since one constraint needs to come from a "true" entanglement for the crossover to take place, hence, the crossover at $N_c \approx 30$ (i.e. where the Rouse and reptation scaling laws intersect in Figure 3.2).

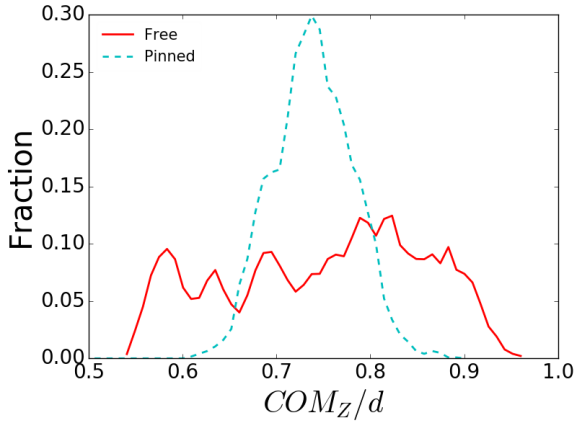

(a)

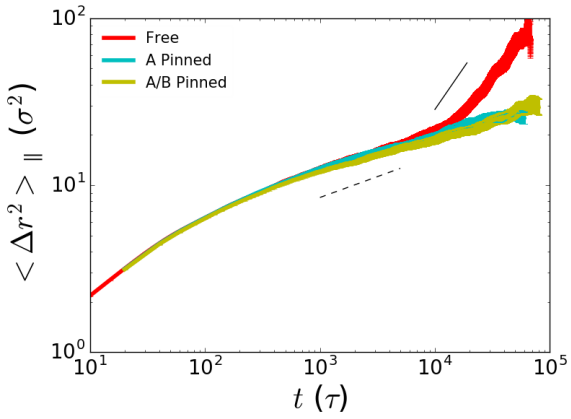

(b)

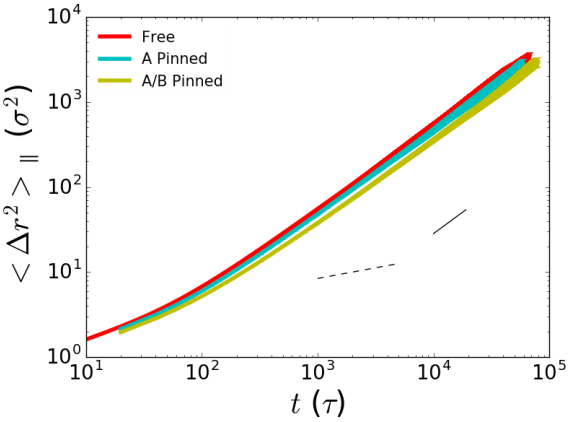

(c)

Figure 3.3: Effect of pinning potential on (a) the COM_z/d profile of one chain for $N = 200$, where the interface is located at $COM_Z/d = 1.0$, and on $\left\langle \Delta r^2 \right\rangle_{\parallel}$ for (b) $N = 200$ and (c) $N = 10$, where solid and dashed lines illustrate t^1 (diffusive motion) and $t^{0.25}$ (entangled motion) scaling, respectively.

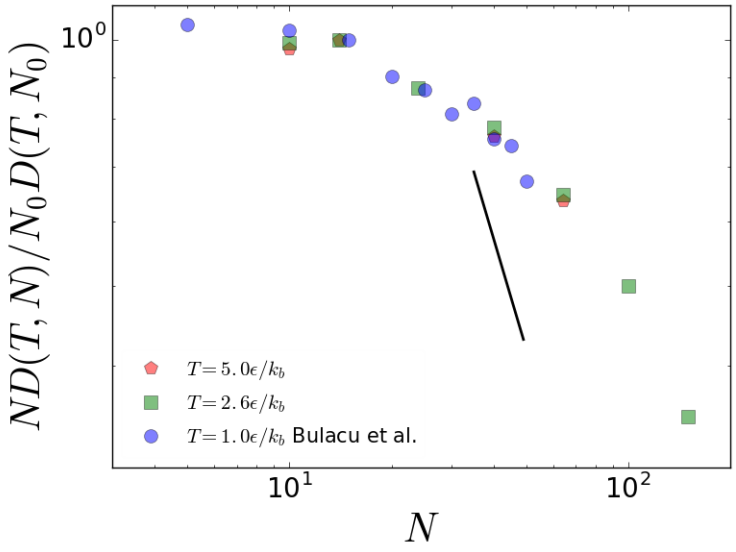

Figure 3.4: Effect of T on the dependence of ND on N for HP. The effect of T is normalized with respect to a reference system ($N_0 = 14$) at the particular T. The solid line represents the reptation scaling ($N^{-1.4}$).

Figure 3.6 shows the $G''_{\alpha\beta}$ and $G'_{\alpha\beta}$ moduli (eqs. 3.4 and 3.5) obtained from oscillatory shear simulations of the L phase. The first intercept (i.e., at small oscillation frequency (ω)) of G' and G'' is related to the entanglements relaxation time (i.e., disentanglement), while the second intersect corresponds to the segment relaxation time between entanglements [23, 80]. Figure 3.6a-c shows that for $L \parallel$ orientation no signs of entanglements are detectable for $N = 10-76$ where beads are expected to experience a nearly homogenous environment. However, in the $L \perp$ and $L\mathcal{T}$ orientations (Figures 3.6d-i) for $N > 40$, an entanglement-like signature in the dynamic oscillatory shear modulus is observed, consistent with the topological constraint effect induced by the interface.

To elucidate whether the modulus plateau of the $L \perp$ and $L\mathcal{T}$ orientations is related to rubbery or cubic-phase behavior, dynamic oscillatory shear simulations of HP with $N = 200$ and 40 were conducted as a referential case pertinent

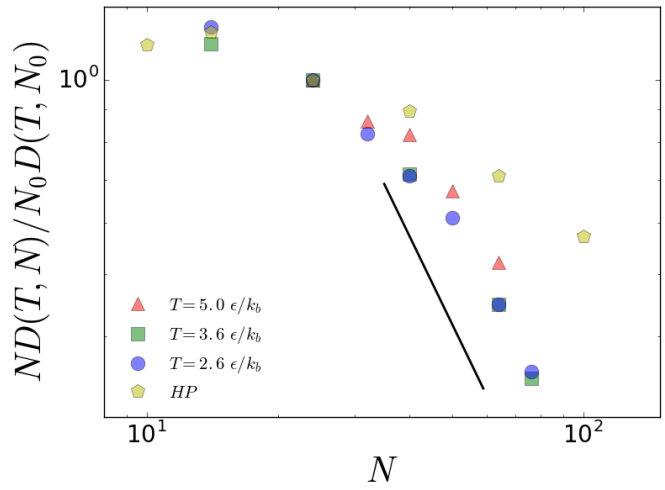

(a)

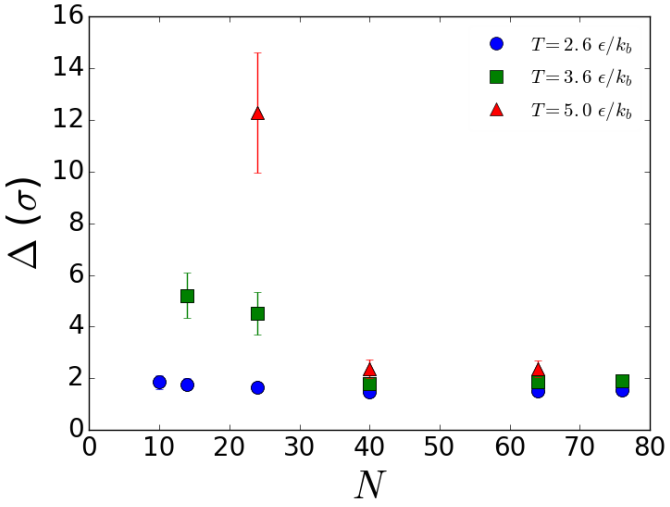

(b)

Figure 3.5: Effect of T on (a) the dependence of ND on N for DBP with L morphology and HP, where the effect of T is normalized with respect to a reference system ($N_0 = 24$) at the particular T, and the solid line represents the reptation scaling ($N^{-1.4}$), and (b) the dependence of Δ^* on N for DBP with L morphology. Error bars represent the standard deviation from the different configurations used in the calculation.

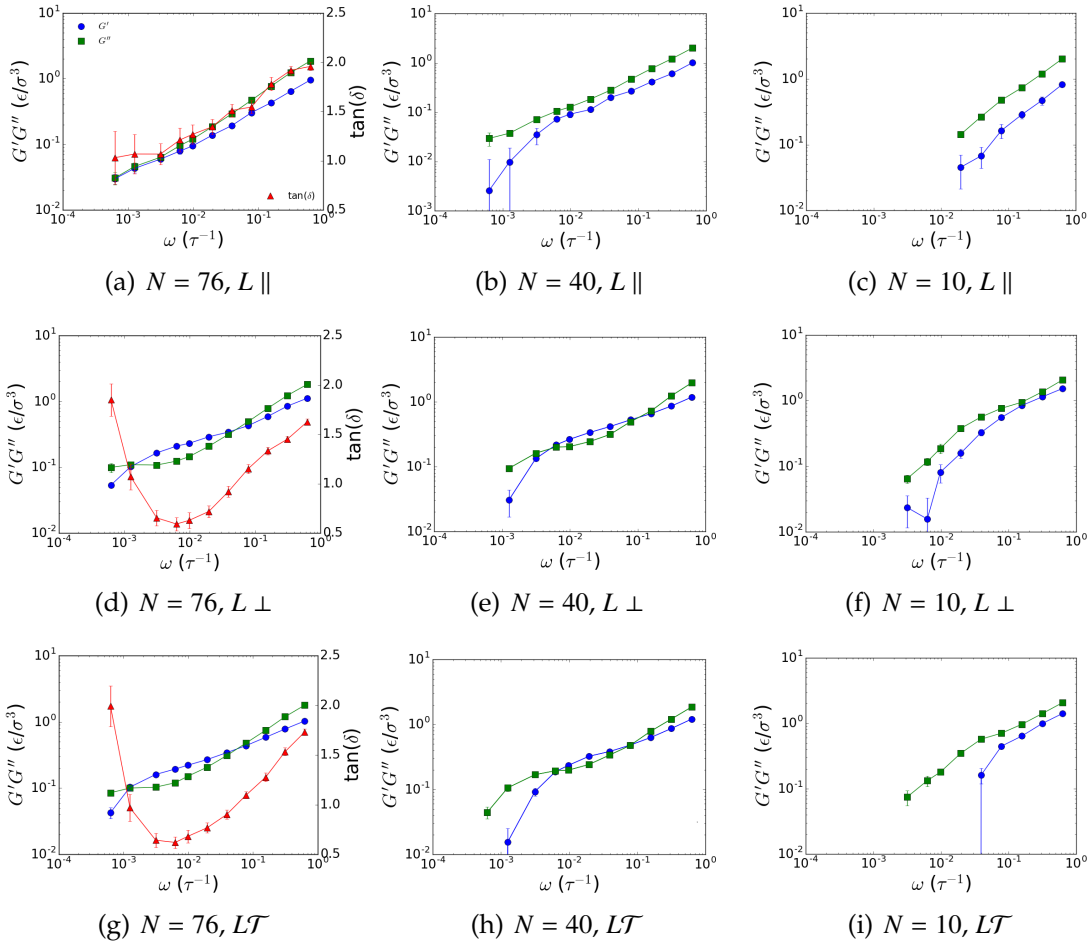

(a) $N = 76$, $L \parallel$ (b) $N = 40$, $L \parallel$ (c) $N = 10$, $L \parallel$

(d) $N = 76$, $L \perp$ (e) $N = 40$, $L \perp$ (f) $N = 10$, $L \perp$

(g) $N = 76$, $L\mathcal{T}$ (h) $N = 40$, $L\mathcal{T}$ (i) $N = 10$, $L\mathcal{T}$

Figure 3.6: Effect of N and oscillation orientation on $G'_{\alpha\beta}$, $G''_{\alpha\beta}$, and $\tan(\delta)$ of DBP with L morphology at $T = 2.6\epsilon/k_b$ and $\gamma_0 = 0.1$. Error bars represent the 95% confidence interval for uncorrelated initial configurations. The legend is the same as in figure a. See Figure 3.1 for shear orientations nomenclature.

to rubbery plateau behavior. The results shown in Figure 3.7 indicate, counter to trends observed in a previous experimental study of randomly oriented L grains [73], that the modulus plateau of the HP is lower in magnitude than the modulus plateau found for the $L \perp$ and $L\mathcal{T}$, and that the onset of the plateau takes place over a similar ω regime. Additionally, for $L \parallel$ with $N = 200$, only one plateau is apparent, similar to the HP case. For HP with $N = 40$, no rubbery plateau is observed, suggesting that the apparent plateau in DBPs for $N < N_e$ is

related to the presence of the interface. We note in passing that our oscillatory shear simulations for the G phase with $N = 18$ confirm the presence of a modulus plateau at terminal frequencies as found in experiments and attributed to the 3D lattice interconnectivity of the block domains [73].

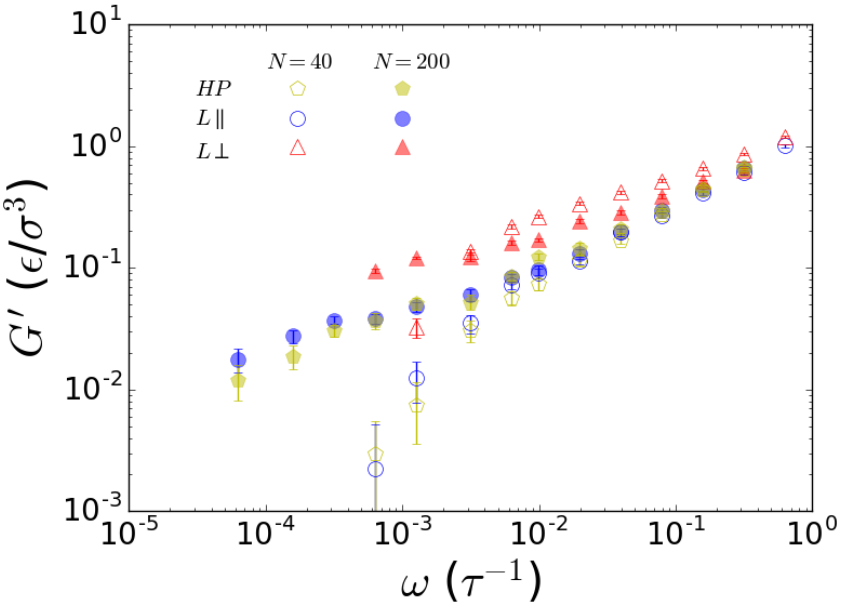

Figure 3.7: $G'_{\alpha\beta}$ of $L \parallel$ and $L \perp$ orientations compared to G' of HP case at $T = 2.63\epsilon/k_b$ for $N = 40$ and $N = 200$ obtained from dynamic oscillatory shear simualtions. Error bars represent the standard error from uncorrelated initial configurations. The results for the $L\mathcal{T}$ orienation, which are similar to that of the $L \perp$ orientation, are not shown for clarity. See Figure 3.1 for shear orientations nomenclature.

To confirm that the range of ω used is wide enough to capture the different relaxation time scales, we tested whether the calculated η reached the Newtonian regime, which is a key tenet in our simulations. We show in Appendix J the mapping of our scaling quantities (m, ϵ, and σ) to a linear polyethylene melt by mapping N_c in our model to experimental data. We then used these scaling quantities to predict D and η for polyethylene and show that they agree with available experimental and atomistic simulations data.

G_N^0 can be related to N_e via the Rubber Elasticity theory [80]:

$$G_N^0 = \frac{4}{5}\frac{\rho k_b T}{N_e} \tag{3.9}$$

resulting in $N_e \approx 11$ for the $L \perp$ and $L\mathcal{T}$ orientations independent of N above 40. At $T = 5.0\epsilon/k_b$, the dynamic oscillatory shear display no signs of a modulus plateau for $N = 40$, whose T_{ODT} is $21\epsilon/k_b$ [28]. These results again confirm that the interface in the strong segregation limit gives rise to an entanglement-like behavior that correlates with the crossover between the Rouse and reptation scaling regimes for D shown in Figure 3.2.

Another important property of polymeric materials that is strongly dictated by entanglements is η_0. In Figure 3.3, we compare η_0 for HP obtained from steady shear simulations to $\eta_{0_{\alpha\beta}}$ for DBPs with L and HC morphologies calculated via steady and dynamic oscillatory shear simulations, and η_0 for Sphere (S) and G morphologies calculated via dynamic oscillatory shear simulations. It can be seen that no signs of reptation can be inferred from the scaling of the trends for all the morphologies and orientations, in agreement with the results from a previous study for homopolymer melts [23]. Figure 3.3 also shows that the viscosity of the $HC \parallel$ and S phases are greater than that in the $L \parallel$ phase, in agreement with a previous study [71]. η_0 for the S phase is smaller than that of $HC \circlearrowleft$, possibly due to its reduced ϕ_1. For $N = 18$, G' of the G phase exhibits a plateau that spans several decades in frequency at low ω (consistant with experimental findings [73]), and as a result, η_0 diverges in the ω range examined. Since the flow direction in the $L \parallel$, $L \perp$, and $HC \parallel$ orientations is not across the interface, we suspect that viscosity differences among them are connected to differences in how chains are aligned relative to the flow direction in the unperturbed state. The larger viscosity values observed for the $HC \circlearrowleft$ and S phases, where the flow direction crosses the interface, likely arises from additional en-

ergetic contributions to the stress response.

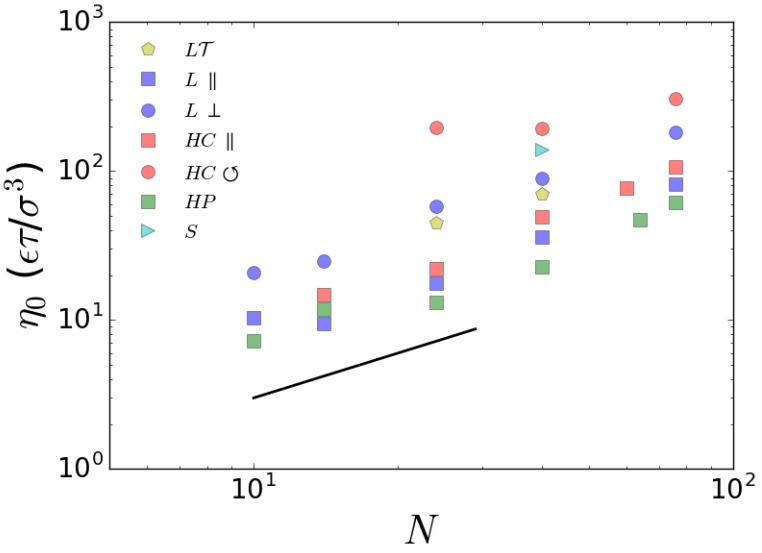

Figure 3.8: $\eta_{0_{\alpha\beta}}$ of DBPs of different morphologies and HP, as a function of shear orientation and N at $T = 2.6\epsilon/k_b$. See Figure 3.1 for shear orientations nomenclature. The straight line represents the Rouse scaling law (N^1).

In the HC and S phases, the majority block conformation is more isotropic, especially on the plane orthogonal to the cylinder axis, compared to the L phase where the blocks are distinctly more stretched in the direction normal to the interface than in the other two directions (parallel to the interface). To corroborate this argument, we show the distribution of the end-to-end distance (R_{ee}) in the three cartesian directions for the L (Figure 3.9a) and HC (Figure 3.9b) morphologies. No difference is observed between the parallel components of R_{ee} in the L phase and individual components of R_{ee} in the HC phase.

In the $L\ \|$ orientation, the shear-flow neutral direction is normal to the interface. Because chains are more aligned in the neutral direction in the $L\ \|$ orientation than in the $HC\ \|$ orientation, chain segments experience less velocity gradient and hence generate a reduced viscosity in the $L\ \|$ orientation compared

to the $HC \parallel$ orientation. Similarly, in the $L \perp$ orientation, the interface-normal direction is the velocity gradient direction, and since chains are more aligned in that direction, the $L \perp$ viscosity is greater than those for the $L \parallel$ and $HC \parallel$ orientations. In Appendix K we further show that uniaxial deformation simulations for the L and HC phases yield stress responses whose trends can be correlated to the same microscopic trends in chains conformations given here to explain the shear simulation results.

3.5 Conclusions

In this work, we examined first the role of DBP microphase separation on the onset of reptation scaling in D. We studied in particular detail the behavior of the diffusivity parallel to the interface in the L morphology. Specifically, we showed that in the strong segregation limit, the DBP interface constrains chain conformations in a way akin to topological constraints caused by entanglements, giving rise to a temperature-dependent early crossover from Rouse to reptation scaling (i.e. $N_c \approx N_e$ *vs.* $N_c \approx 2N_e$ in homopolymers). Similarly, Lai et al. [81] showed that N_c for the lateral diffusion in a polymer brush depends on the grafting density with higher values resulting in earlier crossover. A brush of mobile chains densely grafted to a flat surface, can be likened to a DBP lamellar layer. Moreover, our dynamic oscillatory shear simulations also reveal an entanglement-like signature at the same N_c for the $L \perp$ and $L\mathcal{T}$ orientations.

We also found that the value of N_c for the diffusion coefficient increases with T as the segregation strength decreases in DBPs, in contrast to the T–independent crossover behavior in HP. Our calculations of the interface thick-

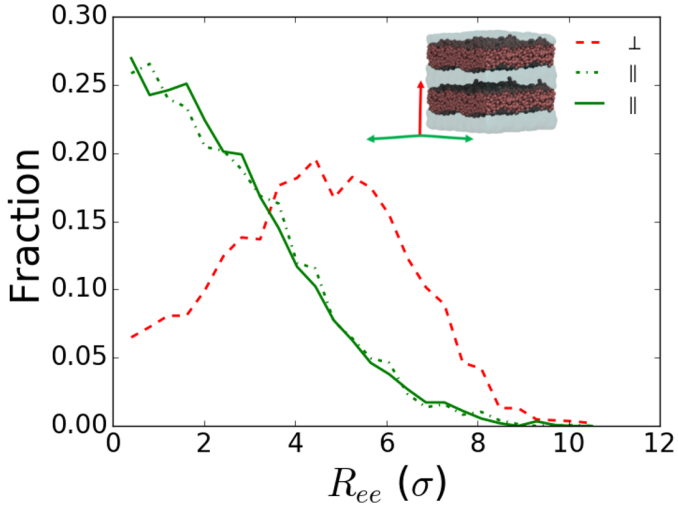

(a) *L*

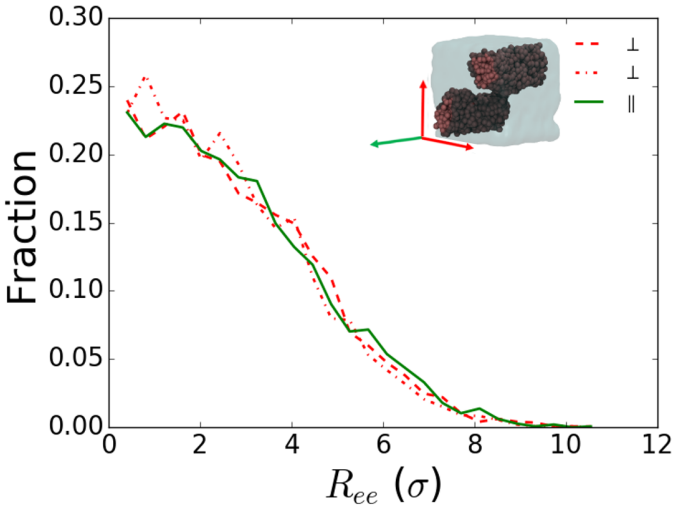

(b) *HC*

Figure 3.9: Distribution of the absolute value of the end-to-end distance of the majority block chains (R_{ee}) in the three cartesian directions for (a) *L* and (b) *HC* morphology with $N = 40$ chains in the unperturbed state. The specific directions probed are depicted in the inset.

ness, which is inversely related with the segregation strength, confirmed that N_c is associated with N at which the interfacial thickness plateaus at a given T. At low T, N_c becomes independent of T since at least two effective topological constraints are needed for the crossover to take place (i.e., one from the interface and at least one from the chain length).

In the entangled regime, we found that block retraction is an important mechanism in the diffusion of chains parallel to the L-phase interface. In simulations designed to suppress fluctuations in chain extension normal to the interface, it was found that the mean square displacement of the interfacial bead in the lateral directions approaches a plateau that is commensurate to the squared diameter of the tube in reptation theory, indicating that block retraction is important to activate lateral diffusion. For chain lengths below N_e, the lateral diffusion was found to be independent of the block retraction motion. More generally, however, lateral diffusion of a given chain is likely a complex process that involves not only its retraction but also the cooperative motion of the surrounding neighbor chains. Further analysis of the effect of neighboring chains will be needed to identify in more detail the underlying mechanism of DBP diffusion in the entangled regime.

Analysis of steady and dynamic oscillatory shear simulations of different morphologies with different orientations revealed that the anisotropic zero-shear viscosity ($\eta_{0_{\alpha\beta}}$) mainly depends on chain alignment with respect to the virtual flow direction in the unperturbed state, exhibiting a reduced value when chains are aligned in the flow or neutral direction. Moreover, the viscosity is always the largest when shear flow is across the interface, likely due to additional energetic contributions associated with the stress response to interfacial defor-

mations.

This work was concerned with describing the anisotropic stress response of DBPs to different modes of deformation (simple shear, oscillatory shear, and uniaxial elongation) and the direction of the deformation relative to orientation of the morphology. This study could be extended in a number of different directions. For example, the uniaxial deformations simulated in this study have mainly probed the rubbery and solid response; however, performing a constant cross-section uniaxial elongation would be informative to probe adhesive properties [82]. Simulations that probe the nano- and micro-rheology of DBP systems would be interesting given the multiple length scales, such as Δ, and domain size, that define the structure of microphase separated morphologies. Such studies would allow to elucidate the interplay between the different length scales and the dynamics of nanoparticle probes with different size and concentration. Such insights would be relevant to understand the rheology of not only DBP melts but also DBP composites and electrolyte systems (whose macro-viscoelastic properties have little influence on the dynamics of the particles or ions [22, 50]). Work related to these topics is currently underway.

CHAPTER 4

CONCLUSIONS AND FUTURE WORK

4.1 Conclusions

Diblock copolymers (DBP) are important and interesting class of polymeric materials due to the various structures they can form by means of self-assembly. The different structures result, by virtue, on unpredictable variations of their properties. DBP has been used in different applications and fields, such as in in energy storage applications to improve the safety and durability of batteries. Optimizing transport and mechanical properties of solid polymer electrolyte (SPE) is essential for enhanced battery performance and sustainable operations. Using Molecular Dynamic (MD) simulations, two main topics were addressed in this thesis. Mainly, correlations between DBP morphology and their ionic mobility (μ), dynamic, and viscoelastic properties were unveiled.

It was found that the microstructure of macroscopically aligned DBP matrix has a significant impact on μ due to three-fold: (i) different morphologies have different extent of microdomain mixing (β) between the conductive and non-conductive domains due to changes in the proximity to the order-disorder transition and volume fraction of the conductive domain (Figure 1.1). It was found that μ and β are inversely related because of the hindered transport in the close proximity to the glassy and energetically unfavorable non-conductive domain; (ii) μ is significantly reduced by the increased tortuosity of the conductive domain in continuous DBP structures at the nano-scale; and (iii) μ is improved in the presence of interfaces within the conductive domain due to the reduced local density. It was shown that μ for various morphologies and chain lengths

(N) can be correlated with the tortuosity factor (λ) of the conductive domain and β via a single universal curve.

Moreover, the dynamic and viscoelastic properties of neat DBP systems with various morphologies and N were studied. It was found that in the strong segregation limit (i.e., high χN), the interface of the DBP imposes topological constraint similar to that of entanglements as manifested in the rheological signature of the polymer obtained from dynamic mechanical analysis. Moreover, compared to the behavior of isotropic melts, the crossover from Rouse to reptation scaling of the self-diffusion coefficient (D) parallel to the DBP interface takes place at a smaller N, an effect that depends on temperature and is more pronounced in the Lamellae morphology than in the Hexagonal Cylinder morphology. Additionally, it was found that in contrast to the behavior for Rouse chains (i.e., $N < N_e$, where N_e is the entanglement N), for entangled melt (i.e., $N \gg N_e$), block retraction is instrumental for chains to diffuse parallel to the interface. Lastly, analysis of the anisotropic viscosity tensor components of the different morphologies revealed that they are mostly effected by the orientation of the chains relative to the shear flow direction, exhibiting reduced values when chains align in the neutral or flow direction.

4.2 Future Work

There are several methods by which rheological information of polymeric materials can be extracted. The conventional method, which was adapted in this thesis, relies on macroscopic deformation to the material. As a result, the macroscopic rheology is dependent upon the macroscopic chain conformation and for

DBP upon structure symmetries. Alternatively, nanoparticles can be used to probe the micro- or nano-rheology depending on the size of the nanoparticle (d_{NP}) compared to the characteristic length scales of the polymer. Thus, the rheology of the medium is related to the self-diffusion coefficient of the nanoparticles.

The diffusion of attractive nanoparticles in homopolymer melt was shown to transition from a macroviscosity dependent regime to a microviscosity dependent regime as the radius of gyration (R_g) becomes larger than d_{NP}. For $d_{NP} > R_g$, the chain relaxation governs the diffusion of nanoparticles; however, for $R_g \gg d_{NP}$, the local environment around the particle is responsible for the diffusion process since its relaxation is much faster than the polymer chain and a chain relaxation is not required for the nanoparticle diffusion to activate [22,50].

The use of this less-invasive method to extract rheological information in nano or micron length scale would unify the analysis across the different DBP morphologies. Additionally, in DBP, the presence of self-separated domains introduces additional length scales, such as the domain size and the interfacial thickness, the effect of which upon the rheology at a small length scale is unknown. Using MD simulations, I plan on studying the effect of morphology on the viscoleastic properties at the nano/micron length scale.

APPENDIX A

ION-POLYMER INTERACTION SIMPLIFICATION

Electrostatic interactions are not explicitly considered in the ion-polymer interactions due to the fact that even for low salt concentration, the dielectric constant of a typical solid polymer electrolyte, such as polyethylene oxide (PEO) is 5-16 [83], which ensures a Debye screening length (λ_D) that is approximately $0.23nm$ at $300K$ and 0.01 [Li]/[PEO]. The Kuhn length of PEO is $0.8nm$ [30], which is the length scale of the system (i.e., polymer bead size $\sim \sigma_{AA} = \sigma_{BB}$). By considering a screened Coulomb interaction potential, such as the Yukawa Potential:

$$U(r_{ij}) = A\frac{e^{-\lambda_d r_{ij}}}{r_{ij}} + U^{WCA}(r_{ij}) \tag{A.1}$$

where A is a fitting energy parameter and r_{ij} is the separation distance between atom i and atom j, we find that the interaction is effectively screened at a separation distance of 2.5 σ as shown in Figure A.1 along with the Lennard Jones (LJ) potential that was used in this study.

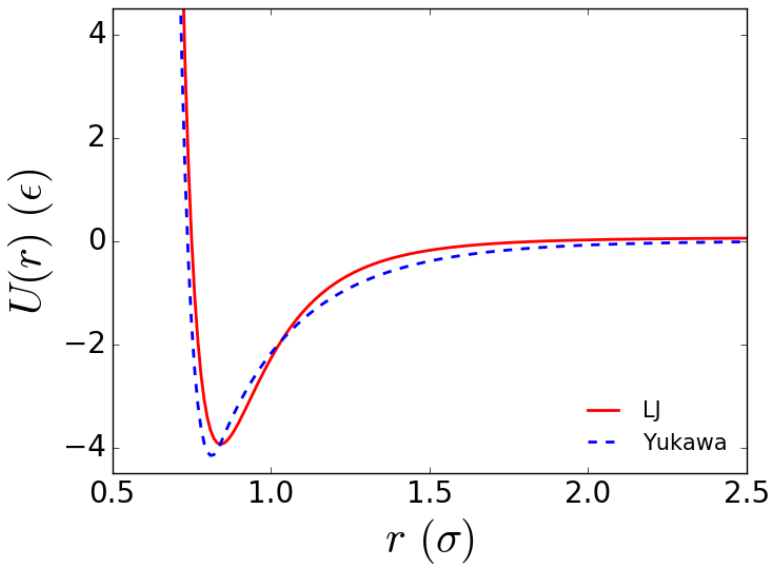

Figure A.1: Comparison of Yukawa potential and Lennard-Jones (LJ) potential for ion-polymer interaction.

APPENDIX B

ION-POLYMER INTERACTION PARAMETERIZATION

On the premise that electrostatic interactions are effectively screened for typical polyelectrolyte systems upon coarse-graining (as discussed in Appendix A), the polymer-ion interaction was assumed to be describable by a LJ interaction potential and calibrated in a Lamellae (L) morphology (i.e., $\phi_1 = 0.5$) due to the ease of characterizing the ions (C) distributions in the polymer and the readily available data in the literature [5]. C ions were effectively trapped in the conductive domain (A) and excluded from the non-conductive domain (B) (as in real systems [5]) for $\epsilon_{AC} = 4.0\epsilon$ as shown in Figure B.1

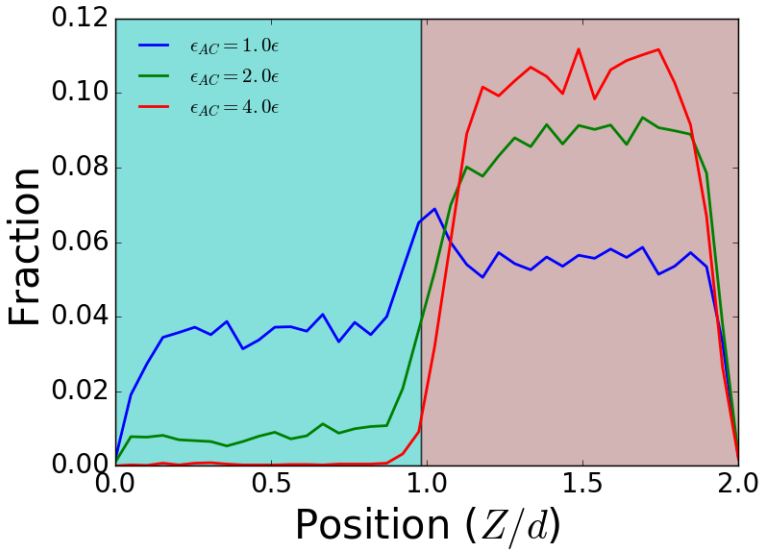

Figure B.1: Effect of interaction strength between A and C (ϵ_{AC}) on the distribution of C in the direction perpendicular to the Lamellae interface (Z) in a DBP system with $N = 40$, where each layer has a thickness $\approx d$. The pink area represents the A domain and cyan area represents the B domain.

APPENDIX C

ION DIFFUSION MECHANISM

Given the degree of coarse graining in the model employed (i.e., 3 PEO monomers per LJ bead given that a PEO monomer is $\approx 0.28nm$ [32]), short-time dynamics associated with atomistic details of intrachain diffusion and C coordination are not captured explicitly in our simulations. However, the long-time diffusive process associated with interchain hopping [19] is captured, which in our systems is attained at a very short time as shown in the dependence of ions displacement (Δx) in the direction of applied external force F on time t, indicative of a dominant interchain diffusion mechanism in Figure C.1.

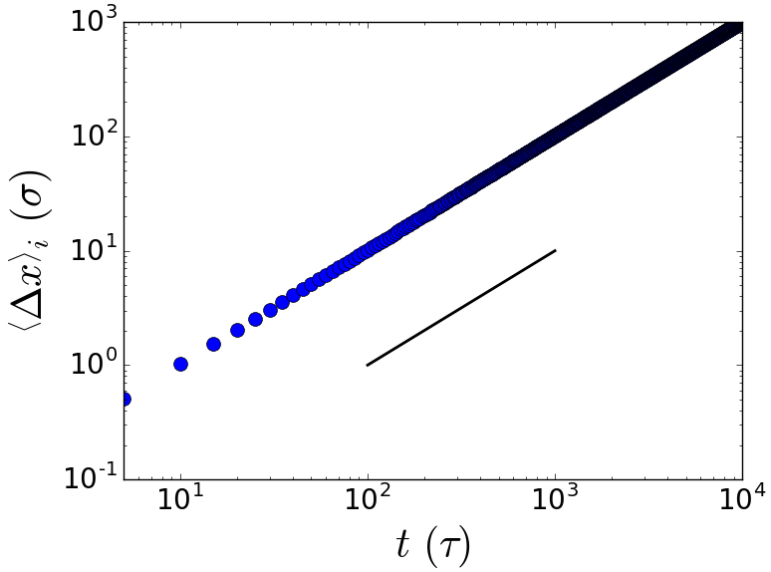

Figure C.1: Ensemble average ions displacement ($\langle \Delta x \rangle_i$) in the direction of applied F for $N = 76$ at $T = 2.63\epsilon/k_b$. Solid line represents the linear scaling.

APPENDIX D

IONIC MOBILITY LINEAR RESPONSE REGIME VERIFICATION

To ensure that under the external force, the ionic mobility is extracted from the linear response regime, a range of force magnitudes (F) in the vicinity of the one used in the study were tested. As shown in Figure D.1, the ensemble average drift velocity ($\langle \Delta v \rangle_i$) in the direction of applied F is linearly related to F.

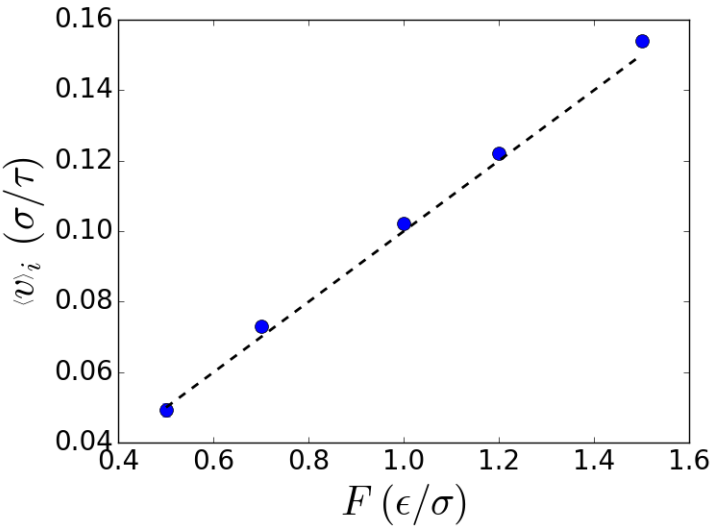

Figure D.1: Effect of F on $\langle \Delta v \rangle_i$ for $N = 14$ at $T = 2.63\epsilon/k_b$

APPENDIX E

EFFECT OF GLOBAL DENSITY ON IONIC MOBILITY

Figure E.1 shows the effect of global density (ρ) on ionic mobility (μ) for two sizes of C (σ_{cc} = 0.25σ and 0.5σ) for comparison.

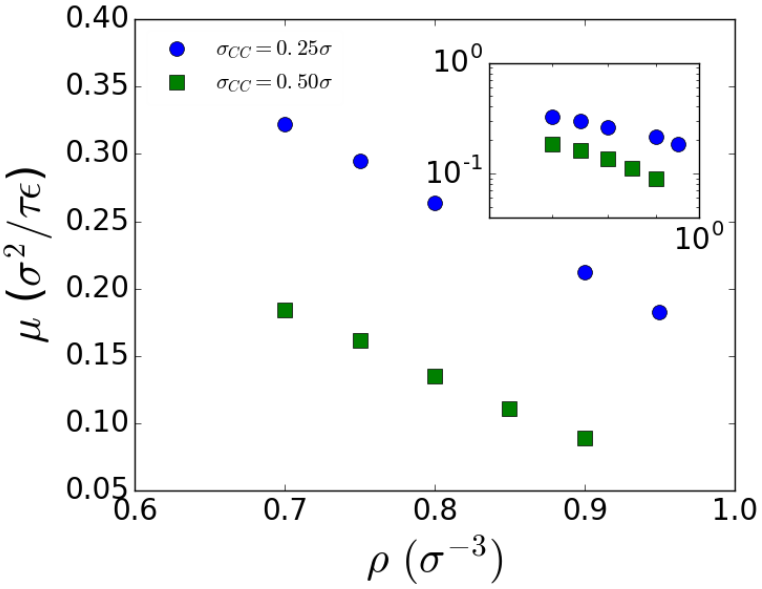

Figure E.1: Effect of ρ on μ for two C sizes (σ_{cc} = 0.25σ and 0.5σ) in homopolymer with N = 40 at T = 2.63ϵ/k_b. A log-log scale plot is shown in the inset.

APPENDIX F

INTERFACIAL THICKNESS CALCULATIONS

The effect of χN (estimated based on Ref. [28]) on the interfacial thickness (Δ^*) of the Lamellae phase was assessed by fitting the order parameter $\psi(z)$ (eq. 3.7) to eq. 3.8. Figure F.1 shows a comparison of Δ^* obtained from the simulations and theory by Semenov [51] (eq. 2.7-2.8) indicating that the simulation results follow approximately the same scaling as the theory with a slight deviation in the actual Δ^*.

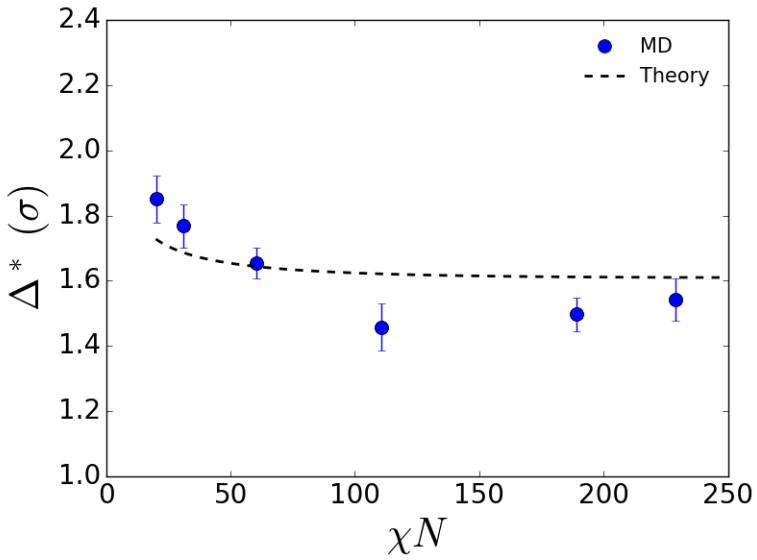

Figure F.1: The dependence of Δ^* on χN from the simulations and theory at fixed $T = 2.63\epsilon/k_b$. Error bars represent the 95% confidence interval from different configurations.

APPENDIX G

TORTUOSITY MEASUREMENT

G.1 Geometric Analysis for Hexagonal Cylinders

The tortuosity of the Hexagonal Cylinder morphology when the majority component is conductive and force is applied perpendicular to the cylinders ($HC_{\perp}$) depends on the diameter of the cylinder ($2r$) and box length (l) (i.e., domain size), which can be related to the chain length (N). Using eq. G.1, the tortuosity was calculated was calculated by finding the average length of the paths travelled by an ion going across the box length, where r^* and σ^*_{BC} are the cylinder radius and the effective interaction diameter between B and C reduced by l, respectively. An effective cylinder diameter was used which includes the interaction cut-off diameter in the BC interaction potential ($2^{1/6}\sigma_{BC}$). The diameter was estimated by taking the projection of all the beads within a cylinder to the two directions normal to the cylinder axis, and calculating the width of the bead distribution in the two directions.

$$\lambda = \left(\frac{\pi \left(r^* + 2^{1/6}\sigma^*_{BC} \right)}{2} - \left(r^* + 2^{1/6}\sigma^*_{BC} \right) + 1 \right) \times 2 \left(r^* + 2^{1/6}\sigma^*_{BC} \right) + 1 - 2 \left(r^* + 2^{1/6}\sigma^*_{BC} \right) \tag{G.1}$$

G.2 Brownian Dynamics for Gyroid Morphology

Since identifying λ for Gyroid when the majority component is conductive (G Maj.) from the geometry of the structure is rather complicated, an alternative

definition of tortuosity is used based on the particle mobility in the tortuous structure of interest relative to that in free-space (i.e., Lamellae) [52]. In order to estimate λ for G Maj., particles were used to probe the tortuosity of the structure by removing the conductive polymer domain, freezing the non-conductive domain, and applying a stochastic thermostat to induce Brownian-like dynamics to decorrelate the trajectories of the particles, particularly important to probe tortuous paths. By doing so, the effect of the interface roughness (already captured by β in the ionic mobility) on the probe particle is minimized, and remove any density inhomogeneity in the conductive domain. The Langevin thermostat was used with a damping parameter of 0.1τ and a temperature of $2.6\epsilon/k_b$ applied to the particles only. An external force $F = 1\epsilon/\sigma$ was applied to bias the motion of the probe particles in the direction of interest to estimate the tortuosity from the distance traveled. The λ obtained from this calculation is comparable, but consistently higher, to the geometric values [52] (Figure G.1) for Lamellae, Hexagonal Cylinder, and Gyroid when the minority component is conductive. For each morphology, the structure corresponding to the longest chain length was used to probe the tortuosity with this method to minimize spurious effects (i.e., confinement and roughness of the interface).

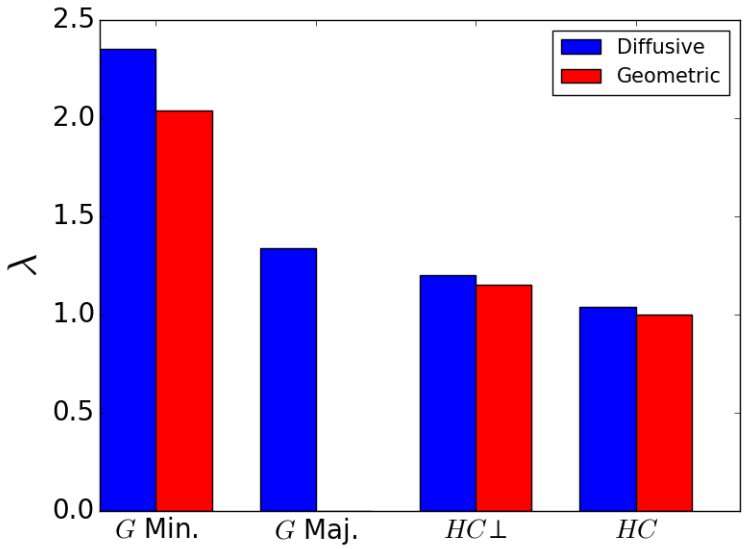

Figure G.1: Comparison of the diffusive and geometric tortuosity factor (λ) for different morphologies.

APPENDIX H

EFFECT OF TEMPERATURE ON IONIC MOBILITY

The effect of T on μ for a representative HP is shown in Figure H.1. This curve is used to rescale μ in DBP to take into account changes in temperature: the ratio of μ in HP between the reference value of $T = 2.63\epsilon/k_b$ and that at the DBP temperature was used in Figure 2.8 of the main text.

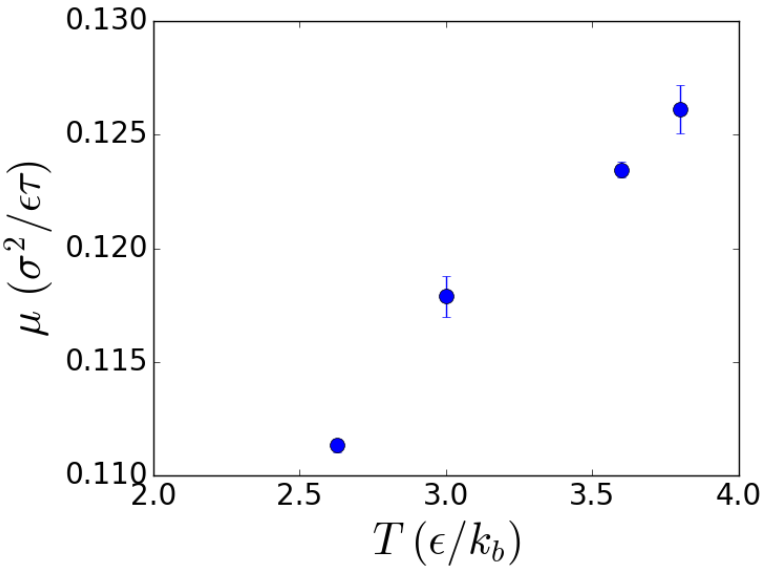

Figure H.1: Effect of T on μ of HP with $N = 40$.

APPENDIX I

COX-MERZ RULE APPLICABILITY

One method to check if the strain amplitude (γ_0) used in dynamic oscillatory shear results in a linear response behavior is by testing the validity of the Cox-Merz Rule. The Cox-Merz Rule is an empirical rule which states that the dependence of the steady shear viscosity (η) on the shear rate ($\dot{\gamma}$) is equivalent to the dependence of the complex viscosity (η^*) on the oscillation frequency (ω) [78]. In our dynamic oscillatory shear simulations, γ_0 was fixed to 10%. As shown in Figure I.1, for chain length $N = 40$, in the perpendicular ($L \perp$) and parallel ($L \parallel$) orientations, the Cox-Merz Rule applies indicating that values from our dynamic oscillatory shear simulations are derived from the linear response regime.

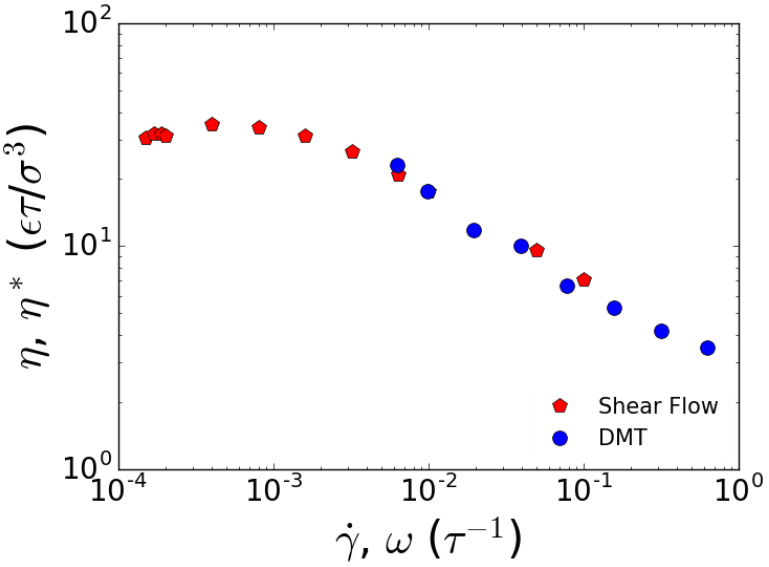

(a) $L \parallel$

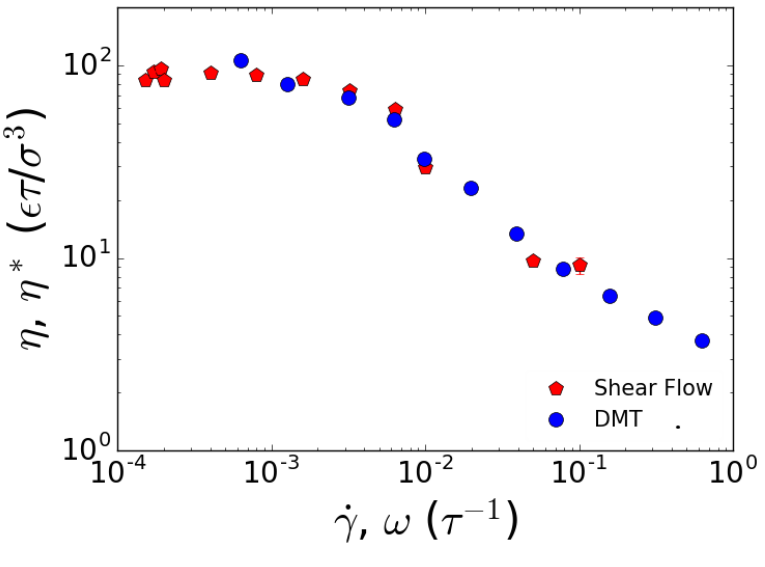

(b) $L \perp$

Figure I.1: The dependence of η on $\dot{\gamma}$ and η^* on ω for a DBP with $N = 40$ at $T = 2.63\epsilon/k_b$ in two orientations (Figure 3.1).

APPENDIX J

SELF-DIFFUSION COEFFICIENT AND ZERO-SHEAR VISCOSITY MAPPING TO POLYETHYLENE

One method of determining if the dynamic oscillatory (and steady) shear simulations are performed for a wide-enough ω (and $\dot{\gamma}$) range to probe experimentally relevant time scales, is to obtain η_0 and dynamic zero-shear viscosity (η_0^*) to confirm that the Newtonian regime is approached. Figure I.1 showed that this was indeed the case, hence indicating that the range used in this study is sufficient to capture the different relaxation modes of the melt.

Moreover, one can map the results obtained from coarse-grained simulations conducted in reduced units into data in real units for specific polymers for which experimental or atomistic simulation results are known, and thus check the level of agreement between the results. By doing so, one also obtains values for the characteristic quantities: m, σ, ϵ, τ. We mapped our results for the self-diffusion coefficient (D) to experimental and atomistic simulations data for linear polyethylene melts [58,84–86] (see Figure J.1a) by matching the crossover molecular-weight (M_c) of D from the Rouse to reptation scaling and the relevant density of the polymer (ρ) and temperature of the experiment (T). Table J.1 lists the characteristic quantities being mapped. Using these quantities, Figure J.1b shows that η_0 results from our simulations are also in good agreement with experimental data of polyethylene.

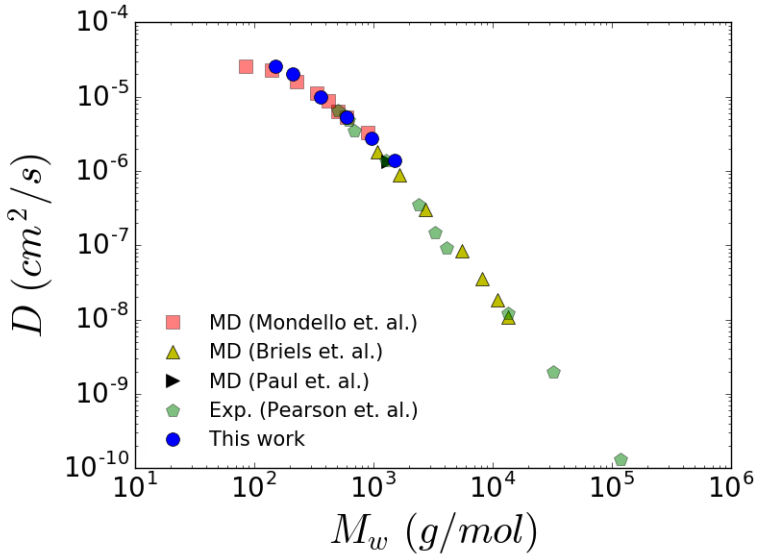

(a)

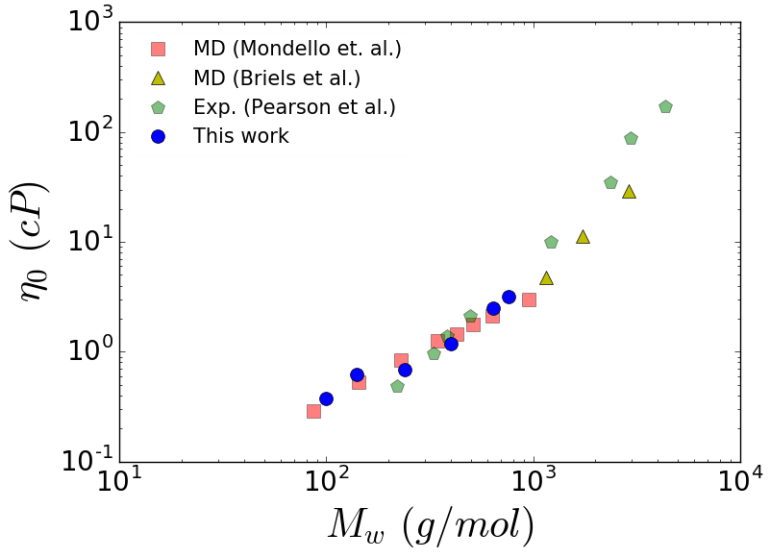

(b)

Figure J.1: Simulation results for (a) D and (b) η_0 from this work mapped to polyethylene using conversion Table J.1. Data from experiments and atomistic simulations are superimposed.

Table J.1: Mapping of characteristic quantities between KG model and polyethylene

Parameter	K-G Model	Polyethylene [85]
ρ	$0.85\sigma^{-3}$	$0.77g/cc$
T	$2.63\epsilon/k_b$	$450K$
M_c	60	$600g/mol$
m	1	$10g/mol$
ϵ	1	$1422J/mol$
τ	1	$9.2 \times 10^{-13}s$
σ	1	$3.5 \times 10^{-8}cm$

APPENDIX K

UNIAXIAL DEFORMATION SIMULATIONS

The mechanical properties of polymeric materials can be characterized from their response to uniaxial deformation. In such experiments, a specimen is elongated in one direction, resulting in the simultaneous sample compression in the directions orthogonal to the elongation direction. Such experiments readily yield the Young's modulus (E), which is a measure of how stiff the material is. The stiffness typically increases for systems whose chains extend in the elongation direction.

To corroborate the argument given in Section 3.4 regarding the correlation between microscopic chain conformations and orientations and the macroscopic anisotropic viscosity, we performed uniaxial deformation simulations of the Lamellae (L) and Hexagonal Cylinder (HC) in the two distinct orientations (Figure K.1) (i.e., parallel and perpendicular directions).

For these simulations a deformation rate of $3.5\times10^{-5}\upsilon/\tau$ was used, where υ is the extension ratio defined as the ratio of the deformed dimension of the box to the initial undeformed state dimension. The stress (σ^*_{ii}) was calculated using eq. K.1, where p_{ii} is the pressure tensor component in the direction of extension, p_{jj} (p_{kk}) is the pressure tensor component in the compression direction, and κ is the Possion's ratio, which is assumed to be 0.5 (a representative value of polymeric materials and appropriate for volume conserving incompressible material [87]).

$$\sigma^*_{ii} = -p_{ii} + \kappa(p_{jj} + p_{kk}) \tag{K.1}$$

E was calculated as the slope from the initial linear part of the stress–strain

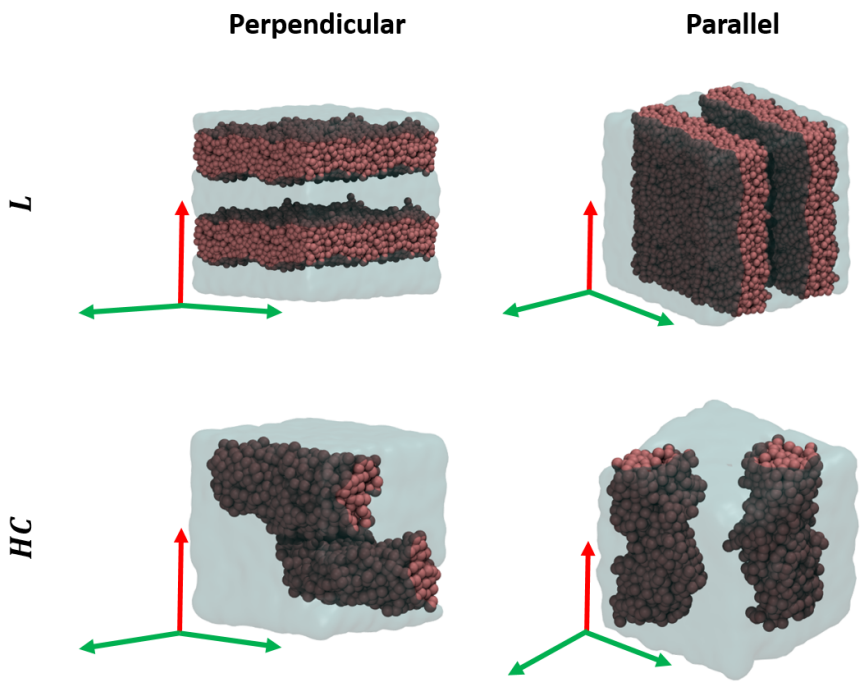

Figure K.1: The different uniaxial flow directions possible for the *L* and *HC* morphologies, where the red arrow represents the extensional direction and the green arrows represent the compression directions.

relation (Figure K.2). In the perpendicular direction, chains in the *L* phase are more aligned in the elongation direction than chains in the *HC* phase, hence, *E* for the perpendicular *L* orientation is larger than that of the perpendicular *HC* orientation. In the parallel direction, both phases have similar *E* value since they have similar alignment (end-to-end distance distribution) in the elongation direction. These results are consistent with the analysis given in Section 3.4 regarding the effect of the chain conformations in the unperturbed state on the anisotropic viscosity trends.

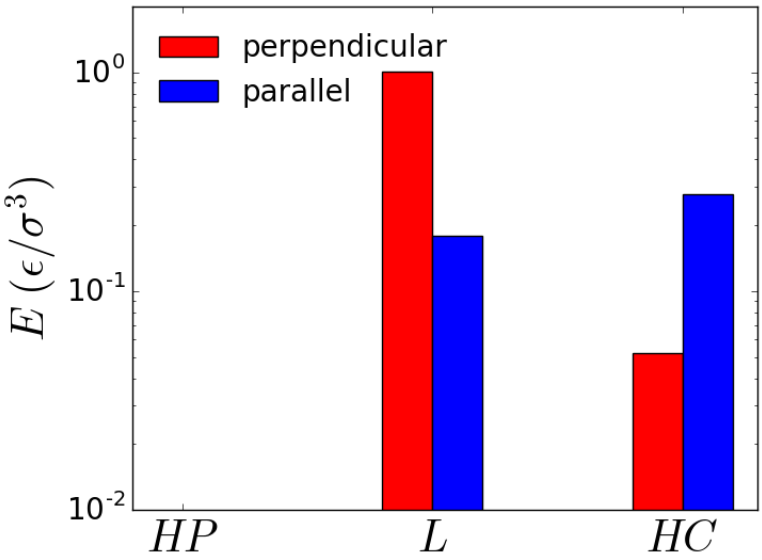

Figure K.2: E obtained from uniaxial deformation for different morphologies having different orientations with respect to the elongation direction (as per Figure K.1), for chain length $N = 40$ and $T = 2.6\epsilon/k_b$.

BIBLIOGRAPHY

[1] M.W. Matsen. Fast and Accurate SCFT Calculations for Periodic Block-Copolymer Morphologies Using the Spectral Method with Anderson Mixing. *The European Physical Journal E*, 30(4):361, dec 2009.

[2] William Humphrey, Andrew Dalke, and Klaus Schulten. VMD: Visual molecular dynamics. *Journal of Molecular Graphics*, 14(1):33–38, feb 1996.

[3] Nikos Hadjichristidis, Stergios Pispas, and George Floudas. *Block Copolymers*. John Wiley & Sons, Inc., Hoboken, USA, nov 2002.

[4] Mukul D. Tikekar, Snehashis Choudhury, Zhengyuan Tu, and Lynden A. Archer. Design Principles for Electrolytes and Interfaces for Stable Lithium-Metal Batteries. *Nature Energy*, 1(9):16114, sep 2016.

[5] Enrique D. Gomez, Ashoutosh Panday, Edward H. Feng, Vincent Chen, Gregory M. Stone, Andrew M. Minor, Christian Kisielowski, Kenneth H. Downing, Oleg Borodin, Grant D. Smith, and Nitash P. Balsara. Effect of Ion Distribution on Conductivity of Block Copolymer Electrolytes. *Nano Letters*, 9(3):1212–1216, mar 2009.

[6] Wen-Shiue Young, Wei-Fan Kuan, and Thomas H. Epps. Block Copolymer Electrolytes for Rechargeable Lithium Batteries. *Journal of Polymer Science Part B: Polymer Physics*, 52(1):1–16, jan 2014.

[7] Ryan L. Weber, Yuesheng Ye, Andrew L. Schmitt, Steven M. Banik, Yossef A. Elabd, and Mahesh K. Mahanthappa. Effect of Nanoscale Morphology on the Conductivity of Polymerized Ionic Liquid Block Copolymers. *Macromolecules*, 44(14):5727–5735, jul 2011.

[8] Hongbo Feng, Xinyi Lu, Weiyu Wang, Nam-Goo Kang, and Jimmy Mays. Block Copolymers: Synthesis, Self-Assembly, and Applications. *Polymers*, 9(12):494, oct 2017.

[9] Ashoutosh Panday, Scott Mullin, Enrique D. Gomez, Nisita Wanakule, Vincent L. Chen, Alexander Hexemer, John Pople, and Nitash P. Balsara. Effect of Molecular Weight and Salt Concentration on Conductivity of Block Copolymer Electrolytes. *Macromolecules*, 42(13):4632–4637, jul 2009.

[10] Venkat Ganesan, Victor Pyramitsyn, Colleen Bertoni, and Manas Shah.

Mechanisms Underlying Ion Transport in Lamellar Block Copolymer Membranes. *ACS Macro Letters*, 1(4):513–518, apr 2012.

[11] Rodger Yuan, Alexander A. Teran, Inna Gurevitch, Scott A. Mullin, Nisita S. Wanakule, and Nitash P. Balsara. Ionic Conductivity of Low Molecular Weight Block Copolymer Electrolytes. *Macromolecules*, 46(3):914–921, feb 2013.

[12] Mahati Chintapalli, X. Chelsea Chen, Jacob L. Thelen, Alexander A. Teran, Xin Wang, Bruce A. Garetz, and Nitash P. Balsara. Effect of Grain Size on the Ionic Conductivity of a Block Copolymer Electrolyte. *Macromolecules*, 47(15):5424–5431, aug 2014.

[13] Wen-Shiue Young and Thomas H. Epps. Ionic Conductivities of Block Copolymer Electrolytes with Various Conducting Pathways: Sample Preparation and Processing Considerations. *Macromolecules*, 45(11):4689–4697, jun 2012.

[14] R C Agrawal and G P Pandey. Solid Polymer Electrolytes: Materials Designing and All-Solid-State Battery Applications: An Overview. *Journal of Physics D: Applied Physics*, 41(22):223001, nov 2008.

[15] C. Berthier, W. Gorecki, M. Minier, M.B. Armand, J.M. Chabagno, and P. Rigaud. Microscopic Investigation of Ionic Conductivity in Alkali Metal Salts-Poly(Ethylene Oxide) Adducts. *Solid State Ionics*, 11:91–95, 1983.

[16] Charles Monroe and John Newman. The Impact of Elastic Deformation on Deposition Kinetics at Lithium/Polymer Interfaces. *Journal of The Electrochemical Society*, 152(2):A396, feb 2005.

[17] Frank S. Bates and Glenn H. Fredrickson. Block Copolymer Thermodynamics: Theory and Experiment. *Annual Review of Physical Chemistry*, 41(1):525–557, oct 1990.

[18] Vaidyanathan Sethuraman, Santosh Mogurampelly, and Venkat Ganesan. Multiscale Simulations of Lamellar PS–PEO Block Copolymers Doped with LiPF6 Ions. *Macromolecules*, 50(11):4542–4554, jun 2017.

[19] Oleg Borodin and Grant D. Smith. Mechanism of Ion Transport in Amorphous Poly(ethylene oxide)/LiTFSI from Molecular Dynamics Simulations. *Macromolecules*, 39(4):1620–1629, feb 2006.

[20] Youngmi Seo, Jonathan R. Brown, and Lisa M. Hall. Diffusion of Selective Penetrants in Interfacially Modified Block Copolymers from Molecular Dynamics Simulations. *ACS Macro Letters*, 6(4):375–380, apr 2017.

[21] Kurt Kremer and Gary S. Grest. Dynamics of Entangled Linear Polymer Melts: A MolecularDynamics Simulation. *The Journal of Chemical Physics*, 92(8):5057–5086, apr 1990.

[22] Jun Liu, Dapeng Cao, and Liqun Zhang. Molecular Dynamics Study on Nanoparticle Diffusion in Polymer Melts: A Test of the Stokes–Einstein Law. *The Journal of Physical Chemistry C*, 112(17):6653–6661, may 2008.

[23] Suchira Sen, Sanat K. Kumar, and Pawel Keblinski. Viscoelastic Properties of Polymer Melts from Equilibrium Molecular Dynamics Simulations. *Macromolecules*, 38(3):650–653, feb 2005.

[24] Vibha Kalra, Fernando Escobedo, and Yong Lak Joo. Effect of Shear on Nanoparticle Dispersion in Polymer Melts: A Coarse-Grained Molecular Dynamics Study. *The Journal of Chemical Physics*, 132(2):024901, jan 2010.

[25] Bernardo M. Aguilera-Mercado, Claude Cohen, and Fernando A. Escobedo. Sawtooth Tensile Response of Model Semiflexible and Block Copolymer Elastomers. *Macromolecules*, 47(2):840–850, jan 2014.

[26] Christian Nowak and Fernando A. Escobedo. Tuning the Sawtooth Tensile Response and Toughness of Multiblock Copolymer Diamond Networks. *Macromolecules*, 49(17):6711–6721, sep 2016.

[27] Christian Nowak and Fernando A. Escobedo. Optimizing the Network Topology of Block Copolymer Liquid Crystal Elastomers for Enhanced Extensibility and Toughness. *Physical Review Materials*, 1(3):035601, aug 2017.

[28] Mark A. Horsch, Zhenli Zhang, Christopher R. Iacovella, and Sharon C. Glotzer. Hydrodynamics and Microphase Ordering in Block Copolymers: Are Hydrodynamics Required for Ordered Phases with Periodicity in More than One Dimension? *The Journal of Chemical Physics*, 121(22):11455, 2004.

[29] Alexandros Chremos, Arash Nikoubashman, and Athanassios Z. Panagiotopoulos. Flory-Huggins Parameter χ, from Binary Mixtures of Lennard-Jones Particles to Block Copolymer Melts. *The Journal of Chemical Physics*, 140(5):054909, feb 2014.

[30] Javier Sacristan, Chunxia Chen, and Janna K. Maranas. Role of Effective Composition on Dynamics of PEO–PMMA Blends. *Macromolecules*, 41(14):5466–5476, jul 2008.

[31] Manjeera Mantina, Adam C Chamberlin, Rosendo Valero, Christopher J Cramer, and Donald G Truhlar. Consistent van der Waals Radii for the Whole Main Group. *The Journal of Physical Chemistry A*, 113(19):5806–5812, may 2009.

[32] S.I. Jeon, J.H. Lee, J.D. Andrade, and P.G. De Gennes. Protein-Surface Interactions in the Presence of Polyethylene Oxide. *Journal of Colloid and Interface Science*, 142(1):149–158, mar 1991.

[33] Mohit Singh, Omolola Odusanya, Gregg M. Wilmes, Hany B. Eitouni, Enrique D. Gomez, Amish J. Patel, Vincent L. Chen, Moon Jeong Park, Panagiota Fragouli, Hermis Iatrou, Nikos Hadjichristidis, David Cookson, and Nitash P. Balsara. Effect of Molecular Weight on the Mechanical and Electrical Properties of Block Copolymer Electrolytes. *Macromolecules*, 40(13):4578–4585, jun 2007.

[34] Steve Plimpton. Fast Parallel Algorithms for Short-Range Molecular Dynamics. *Journal of Computational Physics*, 117(1):1–19, mar 1995.

[35] Joseph E. Basconi and Michael R. Shirts. Effects of Temperature Control Algorithms on Transport Properties and Kinetics in Molecular Dynamics Simulations. *Journal of Chemical Theory and Computation*, 9(7):2887–2899, jul 2013.

[36] James D. Thomin, Pawel Keblinski, and Sanat K. Kumar. Network Effects on the Nonlinear Rheology of Polymer Nanocomposites. *Macromolecules*, 41(16):5988–5991, aug 2008.

[37] M. Murat, G. S. Grest, and K. Kremer. Lamellar Block Copolymers: Diffusion and Reduction of Entanglement Effects. *Europhysics Letters (EPL)*, 42(4):401–406, may 1998.

[38] Michael Murat, Gary S. Grest, and Kurt Kremer. Statics and Dynamics of Symmetric Diblock Copolymers: A Molecular Dynamics Study. *Macromolecules*, 32(3):595–609, feb 1999.

[39] Vibha Kalra, Sergio Mendez, Fernando Escobedo, and Yong Lak Joo. Coarse-grained Molecular Dynamics Simulation on the Placement of

Nanoparticles Within Symmetric Diblock Copolymers Under Shear Flow. *The Journal of Chemical Physics*, 128(16):164909, apr 2008.

[40] Paul J. Flory. Viscosities of Linear Polyesters. An Exact Relationship between Viscosity and Chain Length. *Journal of the American Chemical Society*, 62(5):1057–1070, may 1940.

[41] Bingbing Hong, Fernando Escobedo, and Athanassios Z. Panagiotopoulos. Diffusivities and Viscosities of Poly(ethylene oxide) Oligomers. *Journal of Chemical & Engineering Data*, 55(10):4273–4280, oct 2010.

[42] Andrew J. Schultz, Carol K. Hall, and Jan Genzer. Computer Simulation of Copolymer Phase Behavior. *The Journal of Chemical Physics*, 117(22):10329–10338, dec 2002.

[43] Poornima Padmanabhan, Francisco J. Martinez-Veracoechea, Juan C. Araque, and Fernando A. Escobedo. A Theoretical and Simulation Study of the Self-Assembly of a Binary Blend of Diblock Copolymers. *The Journal of Chemical Physics*, 136(23):234905, jun 2012.

[44] Song Hi Lee and Jayendran C. Rasaiah. Molecular Dynamics Simulation of Ionic Mobility. I. Alkali Metal Cations in Water at 25 C. *The Journal of Chemical Physics*, 101(8):6964–6974, oct 1994.

[45] Daniel Fragiadakis, Shichen Dou, Ralph H. Colby, and James Runt. Molecular Mobility, Ion Mobility, and Mobile Ion Concentration in Poly(ethylene oxide)-Based Polyurethane Ionomers. *Macromolecules*, 41(15):5723–5728, aug 2008.

[46] Ksenia Timachova, Hiroshi Watanabe, and Nitash P. Balsara. Effect of Molecular Weight and Salt Concentration on Ion Transport and the Transference Number in Polymer Electrolytes. *Macromolecules*, 48(21):7882–7888, nov 2015.

[47] Paul J. Flory. Thermodynamics of High Polymer Solutions. *The Journal of Chemical Physics*, 10(1):51–61, jan 1942.

[48] Jiezhu Jin and Jianzhong Wu. A Theoretical Study for Nanoparticle Partitioning in the Lamellae of Diblock Copolymers. *The Journal of Chemical Physics*, 128(7):074901, feb 2008.

[49] Vaidyanathan Sethuraman, Victor Pryamitsyn, and Venkat Ganesan. Influ-

ence of Molecular Weight and Degree of Segregation on Local Segmental Dynamics of Ordered Block Copolymers. *Journal of Polymer Science Part B: Polymer Physics*, 54(9):859–864, may 2016.

[50] S. A. Egorov. Anomalous Nanoparticle Diffusion in Polymer Solutions and Melts: A Mode-Coupling Theory Study. *The Journal of Chemical Physics*, 134(8):084903, feb 2011.

[51] A. N. Semenov. Theory of Block-Copolymer Interfaces in the Strong Segregation Limit. *Macromolecules*, 26:6617–6621, 1993.

[52] Behzad Ghanbarian, Allen G. Hunt, Robert P. Ewing, and Muhammad Sahimi. Tortuosity in Porous Media: A Critical Review. *Soil Science Society of America Journal*, 77(5):1461, 2013.

[53] Aldo Ledesma-Durán, S. I. Hernández, and Iván Santamaría-Holek. Relation between the Porosity and Tortuosity of a Membrane Formed by Disconnected Irregular Pores and the Spatial Diffusion Coefficient of the Fick-Jacobs Model. *Physical Review E*, 95(5):052804, may 2017.

[54] Mark W. Hamersky, Marc A. Hillmyer, Matthew Tirrell, Frank S. Bates, Timothy P. Lodge, and Ernst D. von Meerwall. Block Copolymer Self-Diffusion in the Gyroid and Cylinder Morphologies. *Macromolecules*, 31(16):5363–5370, aug 1998.

[55] S.T. Milner. Polymer Brushes. *Science*, 251(4996):905–914, feb 1991.

[56] P. G. De Gennes. Reptation of a Polymer Chain in the Presence of Fixed Obstacles. *The Journal of Chemical Physics*, 55(2):572–572, 1971.

[57] P. G. De Gennes. Dynamics of Fluctuations and Spinodal Decomposition in Polymer Blends. *The Journal of Chemical Physics*, 72(572):4756–6387, 1980.

[58] D. S. Pearson, G. Ver Strate, E. Von Meerwall, and F. C. Schilling. Viscosity and Self-Diffusion Coefficient of Linear Polyethylene. *Macromolecules*, 20(5):1133–1141, sep 1987.

[59] Eric J. Amis and Charles C. Han. Cooperative and Self-Diffusion of Polymers in Semidilute Solutions by Dynamic Light Scattering. *Polymer*, 23(10):1403–1406, sep 1982.

[60] Craig R. Bartels, Buckley Crist, and William W. Graessley. Self-Diffusion

Coefficient in Melts of Linear Polymers: Chain Length and Temperature Dependence for Hydrogenated Polybutadiene. *Macromolecules*, 17(12):2702–2708, dec 1984.

[61] Carol B. Gell, William W. Graessley, Vasilis Efstratiadis, Marinos Pitsikalis, and Nikos Hadjichristidis. Viscoelasticity and Self-Diffusion in Melts of Entangled Asymmetric Star Polymers. *Journal of Polymer Science: Part B: Polymer Physics*, 35:1943–1954, 1997.

[62] Jacob Klein. Dynamics of Entangled Linear, Branched, and Cyclic Polymers. *Macromolecules*, 19(1):105–118, jan 1986.

[63] Timothy P. Lodge. Reconciliation of the Molecular Weight Dependence of Diffusion and Viscosity in Entangled Polymers. *Physical Review Letters*, 83(16):3218–3221, oct 1999.

[64] T. P. Lodge and M. C. Dalvi. Mechanisms of Chain Diffusion in Lamellar Block Copolymers. *Physical Review Letters*, 75(4):657–660, jul 1995.

[65] M. C. Dalvi, C. E. Eastman, and T. P. Lodge. Diffusion in Microstructured Block Copolymers: Chain Localization and Entanglements. *Physical Review Letters*, 71(16):2591–2594, oct 1993.

[66] Xiaohong Pan and J. Scott Shaffer. Onset of Chain Entanglements in Block Copolymer Lamellae. *Macromolecules*, 29(12):4453–4455, jan 1996.

[67] Vaidyanathan Sethuraman, Dylan Kipp, and Venkat Ganesan. Entanglements in Lamellar Phases of Diblock Copolymers. *Macromolecules*, 48(17):6321–6328, sep 2015.

[68] Abelardo Ramírez-Hernández, Brandon L. Peters, Ludwig Schneider, Marat Andreev, Jay D. Schieber, Marcus Müller, Martin Kröger, and Juan J. de Pablo. A Detailed Examination of the Topological Constraints of Lamellae-Forming Block Copolymers. *Macromolecules*, 51(5):2110–2124, mar 2018.

[69] Arash Nikoubashman, Richard A. Register, and Athanassios Z. Panagiotopoulos. Simulations of Shear-Induced Morphological Transitions in Block Copolymers. *Soft Matter*, 9(42):9960, 2013.

[70] Brandon L. Peters, Abelardo Ramírez-Hernández, Darin Q. Pike, Marcus Müller, and Juan J. de Pablo. Nonequilibrium Simulations of Lamel-

lae Forming Block Copolymers under Steady Shear: A Comparison of Dissipative Particle Dynamics and Brownian Dynamics. *Macromolecules*, 45(19):8109–8116, oct 2012.

[71] Kai Zhang and Charles W. Manke. Simulation of Diblock Copolymer Melts by Dissipative Particle Dynamics. *Computer Physics Communications*, 129(1-3):275–281, jul 2000.

[72] Ji Ho Ryu, Han Sol Wee, and Won Bo Lee. Molecular Dynamics Study on Microstructures of Diblock Copolymer Melts with Soft Potential and Potential Recovery. *Physical Review E*, 94(3):032501, sep 2016.

[73] M. B. Kossuth, D. C. Morse, and F. S. Bates. Viscoelastic Behavior of Cubic Phases in Block Copolymer Melts. *Journal of Rheology*, 43(1):167–196, 1999.

[74] Mihail Vladkov and Jean-Louis Barrat. Linear and Nonlinear Viscoelasticity of a Model Unentangled Polymer Melt: Molecular Dynamics and Rouse Modes Analysis. *Macromolecular Theory and Simulations*, 15(3):252–262, apr 2006.

[75] Francisco J. Martínez-Veracoechea and Fernando A. Escobedo. Simulation of the Gyroid Phase in Off-Lattice Models of Pure Diblock Copolymer Melts. *The Journal of Chemical Physics*, 125(10):104907, sep 2006.

[76] A. Einstein. Über die von der Molekularkinetischen Theorie der Wärme Geforderte Bewegung von in Ruhenden Flüssigkeiten Suspendierten Teilchen. *Annalen der Physik*, 322(8):549–560, 1905.

[77] Denis J. Evans and G. P. Morriss. Nonlinear-Response Theory for Steady Planar Couette Flow. *Physical Review A*, 30(3):1528–1530, sep 1984.

[78] W. P. Cox and E. H. Merz. Correlation of Dynamic and Steady Fow Viscosities. *Journal of Polymer Science*, 28(118):619–622, apr 1958.

[79] Monica Bulacu and Erik van der Giessen. Molecular-Dynamics Simulation Study of the Glass Transition in Amorphous Polymers with Controlled Chain Stiffness. *Physical Review E*, 76(1):011807, jul 2007.

[80] Chenyang Liu, Jiasong He, Evelyne Van Ruymbeke, Roland Keunings, and Christian Bailly. Evaluation of Different Methods for the Determination of the Plateau Modulus and the Entanglement Molecular Weight. *Polymer*, 47(13):4461–4479, 2006.

[81] Pik-Yin Lai and Kurt Binder. Structure and Dynamics of Grafted Polymer Layers: A Monte Carlo Simulation. *The Journal of Chemical Physics*, 95(124):4379–4423, 1991.

[82] Sushmit Goyal and Fernando A. Escobedo. Structure and Transport Properties of Polymer Grafted Nanoparticles. *The Journal of Chemical Physics*, 135(18):184902, nov 2011.

[83] S.M. Ansari, M. Brodwin, M. Stainer, S.D. Druger, M.A. Ratner, and D.F. Shriver. Conductivity and Dielectric Constant of the Polymeric Solid Electrolyte, (PEO)8NH4SO3CF3, in the 100 Hz to 1010 Hz Range. *Solid State Iortics*, 17:101–106, 1985.

[84] Maurizio Mondello and Gary S. Grest. Molecular Dynamics of Linear and Branched Alkanes. *The Journal of Chemical Physics*, 103(16):7156–7165, oct 1995.

[85] J. T. Padding and W. J. Briels. Time and Length Scales of Polymer Melts Studied by Coarse-Grained Molecular Dynamics Simulations. *The Journal of Chemical Physics*, 117(2):925–943, jul 2002.

[86] W. Paul, Grant D. Smith, and Do Y. Yoon. Static and Dynamic Properties of a n-C100H202 Melt from Molecular Dynamics Simulations. *Macromolecules*, 30(25):7772–7780, dec 1997.

[87] G. N. Greaves, A. L. Greer, R. S. Lakes, and T. Rouxel. Poisson's Ratio and Modern Materials. *Nature Materials*, 10(11):823–837, oct 2011.